Bulk Magnetic Measurements on Single Crystal $La_{0.73}Ba_{0.27}MnO_3$ and Polycrystalline $La_{0.5}Sr_{0.5}CoO_3$

by

Tyler Brown

A thesis submitted to the Faculty of Graduate Studies of

The University of Manitoba

in partial fulfilment of the requirements of the degree of

MASTER OF SCIENCE

Department of Physics and Astronomy

University of Manitoba

Winnipeg

THE UNIVERSITY OF MANITOBA

FACULTY OF GRADUATE STUDIES

*****

COPYRIGHT PERMISSION

Bulk Magnetic Measurements on Single Crystal $La_{0.73}Ba_{0.27}MnO_3$ and Polycrystalline $La_{0.5}Sr_{0.5}CoO_3$

BY

Tyler Brown

A Thesis/Practicum submitted to the Faculty of Graduate Studies of The University of Manitoba in partial fulfillment of the requirement of the degree

Of

Master of Science

Abstract

This thesis presents the results of two principal studies. In the first, results from detailed magnetization measurements made on a single crystal sample of $La_{0.73}Ba_{0.27}MnO_3$ are presented. Analysis of the spontaneous magnetization shows a reduction in this property below 60 K which is consistent with a moment reduction in the material. In the second, estimates of the magnetic anisotropy have been made from analysis of the approach to magnetic saturation in the single crystal as well as in polycrystalline $La_{0.5}Sr_{0.5}CoO_3$. These estimates have been compared with those found from coercive field measurements. The analysis shows an order-of-magnitude discrepancy between the two methods.

Contents

Chapter One

1 Introduction

The discovery or rediscovery of colossal magnetoresistance (CMR) in the transition metal oxides has caused considerable effort to be directed toward the understanding of the properties of these materials, as outlined in a recent review [1]. As shown below, the CMR phenomenon is highlighted by a drastic drop in a materials resistivity by application of a magnetic field. In typical metals such a drop would be around 1%, but in CMR materials this reduction can be orders of magnitude [1]. This drastic drop in resistivity makes CMR materials useful in read/write devices.

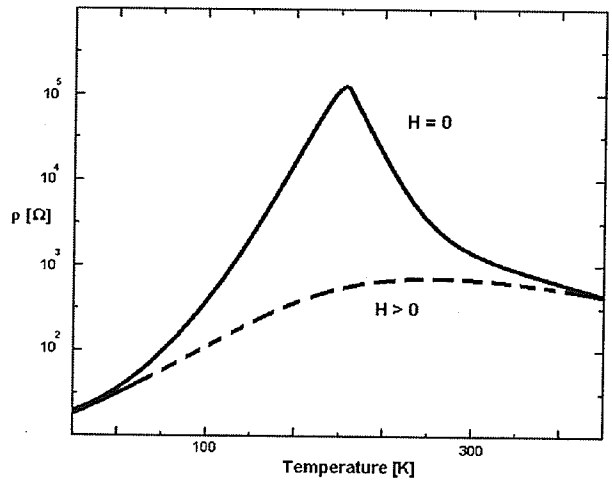

Figure 1.1: *A schematic representation of the resistivity as a function of temperature in CMR materials.*

In terms of possible explanations of this effect, the result that in the manganites the transition from conductor (positively sloped ρ) to insulator (negative sloped ρ) frequently occurs near a ferromagnetic/paramagnetic boundary, as shown below, likely indicates a strong coupling between transport and magnetic behaviour.

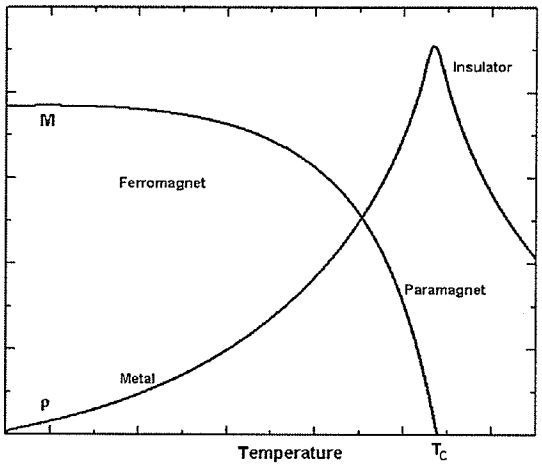

Figure 1.2: *The temperature dependence of the resistivity ρ and the low field magnetization M, in a typical CMR material.*

1.1 The $La_{1-x}R_xMnO_3$ System

Manganites of the form $La_{1-x}R_xMnO_3$, where R is divalent cation (Ca, Sr, Ba, etc), were first grown by Jonker and Van Santen [2, 3] in 1950. Through x-ray diffraction they were able to determine that the system had a perovskite structure. An ideally cubic perovskite structure is shown in Figure 1.3. Manganese ions form a simple cubic lattice with oxygen ions being centered on the cube edges. The La ions, or their substitutionary replacement, are positioned at the center of the cube. The so-called MnO_6 octahedron are also shown.

While CMR is not the focus of this thesis, it is the motivation for the study of the manganites and as such deserves to be discussed in some detail.

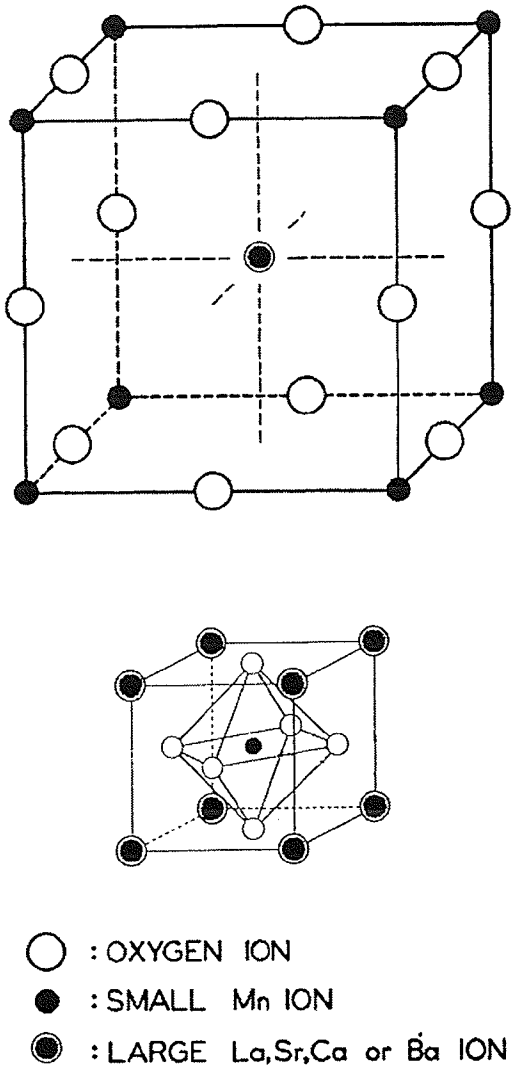

Figure 1.3: *Above, the ideal cubic $LaBaMnO_3$ structure with a perovskite lattice. Below, a MnO_6 octahedron.*

1.2 Double Exchange

Proposed by Zener [4] in 1951, double exchange is a mechanism meant to explain the existence of ferromagnetism and electrical conductivity change in compounds of manganese with perovskite structure.

The compounds studied were of the form $La_{1-x}A_xMnO_3$ with A representing Ca, Sr, or Ba. Compounds having x of 0 or 1 were found to be non-ferromagnetic. Intermediate values of x resulted in the strongest ferromagnetism, with maximum ordering temperatures occurring in compositions having $0.2 < x < 0.4$, so-called optimally doped materials.

It was shown by Jonker and Van Santen [2, 3] that the affinity of oxygen atoms for two electrons is great enough that the oxygen present in the compounds will be doubly charged, independent of A and x. In the case of $x = 0$, this results in the ionic composition: $La^{3+}Mn^{3+}O_3^{2-}$. When a percentage of the La^{3+} ions are replaced by atoms possessing only two valence electrons, such as Ba or Sr, a corresponding number of Mn^{3+} ions must become Mn^{4+}.

The distribution of Mn^{3+} and Mn^{4+} ions throughout the lattice provides a mechanism that facilitates electrical conduction. This conduction is possible through the exchange of an electron from a Mn^{3+} ion to a Mn^{4+} ion. This electron exchange is not direct though, as the distance between Mn ions is large enough that there is no appreciable wavefunction overlap. It is the intermediate placement of an O^{2-} ion that allows the exchange to take place.

The five-fold orbitally degenerate 3d level of the Mn ions is split by a cubic crystal field, resulting in a lower-lying three-fold degenerate t_{2g} state and an e_g doublet. Due to a strong Hund's rule coupling, not only are the spin-down states at much higher energy, but also the parallel alignment of the spin of an electron in the e_g state with that of the core electrons in the t_{2g} state is energetically favourable. As pictured

below, the electron in the e_g level of the Mn^{3+} ion is able to hop to the 2p site on the O^{2-} ion. Simultaneously, a 2p electron from the O^{2-} ion hops to the e_g site on the Mn^{4+} ion hence the description, double exchange. No mechanism exists which would allow the spin of the e_g electron to switch orientations during the hopping process depicted below.

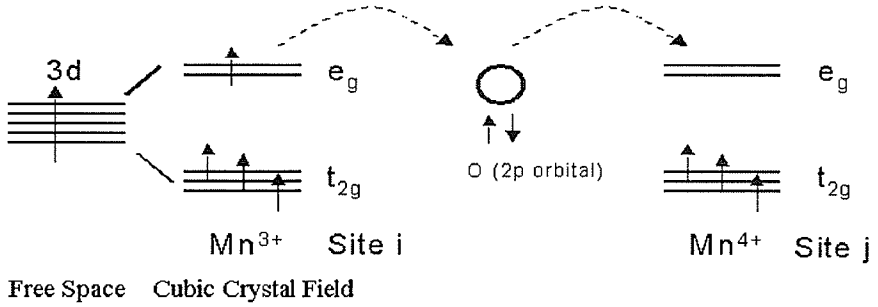

Figure 1.4: *The double exchange process.*

In the paramagnetic state the spin of the core t_{2g} states are randomly aligned. As summarized below, there is a weak chance that hopping will take place if the spin of the electron in the Mn^{3+} e_g state is nearly antiparallel to the core electrons in the Mn^{4+}ion due to the strong Hund's rule coupling mentioned above. The closer to parallel the Mn^{3+} e_g electron spin is to the core spin, the greater the chance of hopping taking place.

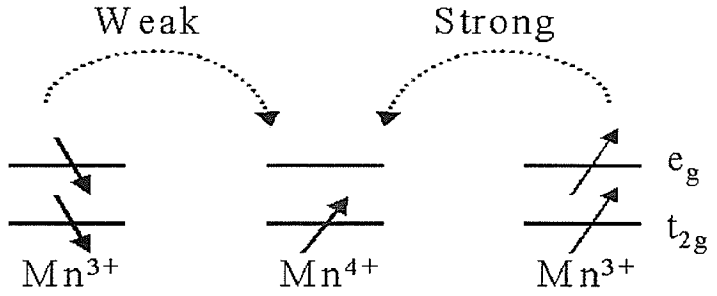

Figure 1.5: *A representation of the effect of Hund's rule coupling on double exchange.*

The probability of electron transfer taking place is thus represented by the transfer integral [5]

$$t_{ij} = b\cos\left(\frac{\Theta_{ij}}{2}\right)$$

where Θ_{ij} represents the angle between the core t_{2g} spins at lattice sites i and j. When the core spins are parallel $\Theta_{ij} = 0$ and $t_{ij} = b$. When the spins are anti-parallel $\Theta_{ij} = \pi$ and $t_{ij} = 0$. The probability of hopping occurring therefore decreases from the maximum as Θ_{ij} rotates from 0 to π.

The effective spin transfer resulting from double exchange also leads to a magnetic coupling between neighbouring Mn spins which exhibits the same angular dependence viz. $\cos\left(\frac{\Theta_{ij}}{2}\right)$. This contrasts with the $\cos(\Theta_{ij})$ dependence exhibited by conventional direct exchange and super exchange. Double exchange can also help to explain the electrical conductivity. When the crystal is in the ferromagnetic phase, the core spins are aligned and hopping of electrons can take place with a high probability allowing easy conduction of electrons.

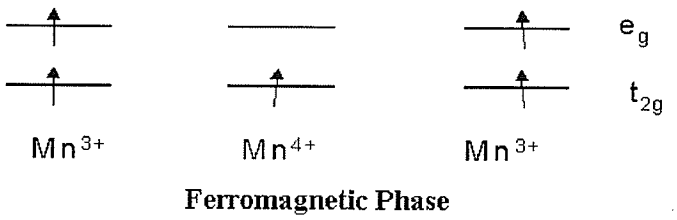

Figure 1.6: *In the ferromagnetic phase core spins are aligned enhancing the conduction process for electrons.*

Above T_C, the crystal is no longer ferromagnetic and the core spins are no longer aligned. The probability of hopping is greatly reduced which leads to a large resistivity in the material.

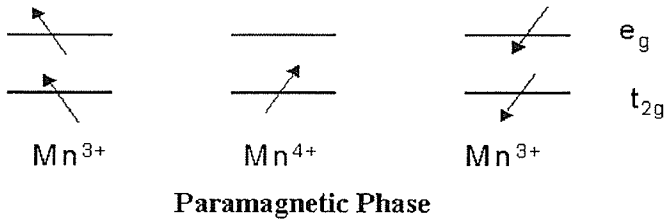

Figure 1.7: *In the paramagnetic phase core spins are no longer aligned and conduction is reduced.*

However, a moderate magnetic field applied near T_C can result in a significant alignment of the t_{2g} core spins, with an attendant increase (decrease) in the hopping probability (resistivity) thus providing a qualitative explanation of the CMR phenomenon, which was considered appropriate for many years.

1.3 Spin Canting

Another early prediction concerning the behaviour of manganites with low doping was made in 1960 by De Gennes [5], who found that the dependence of the transfer electron on the angle between the Mn ions was of serious importance. The energy of the transfer electron becomes lowered if the sublattices become canted and the arrangement is more stable.

A Mn^{3+} ion can have either another Mn^{3+} ion or an Mn^{4+} ion as a neighbour. If the neighbour is another Mn^{3+}, electrons are transferred via super-exchange. Electrons in the t_{2g} state of each ion exchange through an intermediate oxygen. Super exchange shows a strong $Mn-O-Mn$ bond length and bond angle dependence. The sign of the exchange is governed by the Anderson-Goodenough-Kanamori rules [6, 7, 8]. In undoped $LaMnO_3$ the slight distortion from cubic symmetry results in a slightly different $Mn-O-Mn$ bond length/angle within planes compared to between planes.

Here super exchange is dominant but the sign of the super exchange coupling, due to bond length/angle dependence, is positive within planes but negative between planes, leading to the layered antiferromagnetic structure shown below.

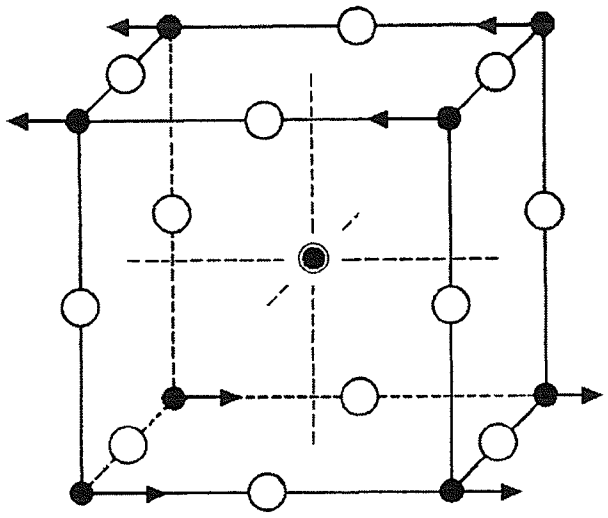

Figure 1.8: *Layered antiferromagnetic structure of* $LaMnO_3$.

In doped systems, De Gennes expressed the super exchange energy as

$$E_{super} = -Nz'J'S^2 + Nz\,|J|\,S^2\cos\Theta, \tag{1}$$

where N represents the number of magnetic ions per unit volume, z' is the number of neighbouring spins within the same antiferromagnetic layer and S is the magnitude of the spin vector. z is the number of neighbouring spins in adjacent layers. J and J' represent the exchange integrals with $J < 0$ and $J' > 0$. The $\cos\Theta$ term represents the conventional angular dependence of the exchange.

If the neighbour is an Mn^{4+}, electrons are transferred via double exchange as previously discussed.

De Gennes was able to determine the canting angle by the minimization of the sum of the super-exchange and double exchange energies. The super-exchange term is represented by Eq. (1) above.

The double exchange term is shown by

$$E_{double} = N \cdot x \left[-z'b' - zb\cos\left(\frac{\Theta}{2}\right) \right], \tag{2}$$

where $N \cdot x$ is the number of transfer electrons, b and b' are the maximum values of the transfer integrals for adjacent layer and inner-layer spins, respectively.

Minimizing the sums of Eq. (1) and Eq. (2) with respect to Θ gives the canting angle Θ_0 as

$$\cos\left(\frac{\Theta_0}{2}\right) = \frac{bx}{4\,|J|\,S^2}.$$

1.4 Current Models for CMR

While the qualitative double exchange picture presented earlier was accepted as an explanation of the CMR effect for many years, recent calculations have revealed several inadequacies. CMR effects are currently viewed as being described by the following two approaches.

1.4.1 Disorder, Phase Separation and Percolation

Disorder in the manganites is caused by the difference in radii between the original A-site La^{3+} cation and the replacement R^{2+} cation. The disorder results in the displacement of the oxygen ions from the original crystallographic positions [9]. Disorder can effectively drive a first order transition to a second order transition [10].

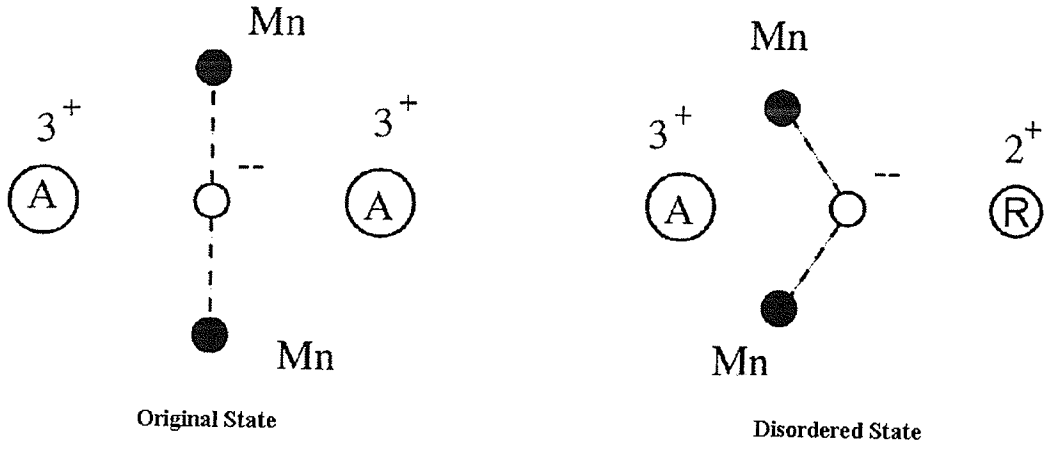

Figure 1.9: *Schematic representation of disorder caused by substitution of* La^{3+} *with an* R^{2+} *cation.*

Calculations of the transition temperature (T_m) from ferromagnetic conducting to paramagnetic insulating states based on double exchange alone give much too large values of T_m. The deformation of the MnO_6 octahedron caused by disorder behaves like a "preformed Jahn-Teller distortion" which serves to localize the e_g electrons. The inclusion of this effect in the calculations of T_m results in much more practical values in the range of experimental findings.

The disorder as described above, is an important factor in observed phase separation. The existence of clusters, or large areas of the material exhibiting either ferromagnetic/metallic or antiferromagnetic/insulating properties, seems to be an intrinsic property of manganites, even appearing in single crystals [11].

Originally it was believed that the clustering was caused by long range Coulomb interactions, which would result in nanometer sized clusters. Work done by Uehara et al. [12] on the system $(La_{5/8-y}Pr_y)Ca_{3/8}MnO_3$ showed the existence of micrometer

sized clusters, suggesting another mechanism. Moreo et al. [10] suggest a disorder-induced phase separation. In samples without disorder the metal-insulator transition is abrupt. When disorder is introduced the two phases can now coexist in clustered regions. The smaller the disorder the larger the cluster size.

When a external field is applied to the cluster, percolation occurs. Shown below is the result of a Monte Carlo simulation by Moreo et al. which clearly illustrates percolation. The dark regions represent metal phased clusters and the white regions are insulator phased clusters when there is no external field. The gray regions represent areas which were insulating in no external field but have become metallic when the field is raised above zero.

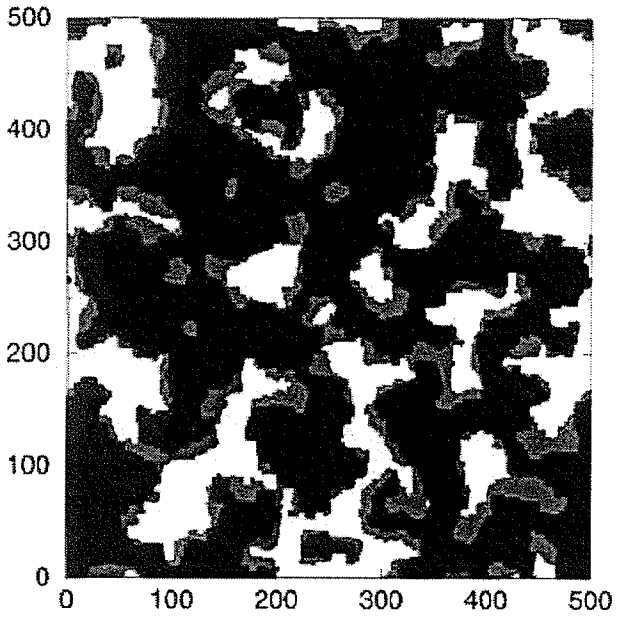

Figure 1.10: *Monte Carlo simulation by Moreo et al. [10] demonstrating percolation in a phase-separated sample.*

In this model then, CMR effects reflect field-induced percolation.

1.4.2 Polarons

An electron in a crystal lattice can effectively deform the lattice through it's attraction/repulsion of ions [13]. This deformation tends to travel through the lattice with the electron and this new "particle" is given the name polaron. Alexandrov and Bratovsky [14] suggest that it is energetically favourable in manganites for the polarons to exist in pairs, or bipolarons, with one having electron spin up and the other spin down. An alternate explanation for the existence of CMR has been introduced by Alexandrov and Bratovsky proposing that it is the breaking of these bipolarons that leads to CMR. In cubic manganites, the bipolaron pairs are essentially immobile due to strong electron-phonon interactions, leading to a high resistance. In the ferromagnetic phase, the bipolarons are effectively split as the polaron spins are aligned and forced to break apart. The polarons are now able to move with ease, substantially lowering the resistance of the material. In this model, depending on the polaron density, the magnetic transition can be either first (discontinuous) or second (continuous) order, which mimics the effects proposed for disorder in these systems [15].

Chapter Two

2 Theoretical Background

2.1 Spontaneous Magnetization

Ferromagnetic materials can be envisioned as a collection of magnetic cells. The atoms within these cells, or *domains*, are spin aligned resulting in a net (spontaneous) magnetic moment. Other terms in the free energy of a system usually cause domain moments to be misaligned, but this can sometimes be overcome by low applied fields, resulting in the material obtaining a net (remanent) magnetization even in the absence of a external magnetic field. The spontaneous, intradomain magnetization of a material is temperature dependent, as an increase in temperature causes thermal agitation between and within domains, and the parallel alignment is broken. Increasing temperature results in increased departure from alignment by the domains and at a characteristic point, the Curie temperature T_C, the alignment becomes random and all spontaneous magnetization is lost in the material. When the material is cooled below this temperature, the spins are able to realign and the spontaneous magnetization is recovered.

The following four topics within the field of ferromagnetics play an important role in subsequent data analysis.

2.2 Spin Wave Theory

In many ferromagnetic materials the spontaneous magnetization below $\frac{T_C}{2}$ results predominately from acoustic mode spin-wave excitations described by the gapped dispersion relation

$$\hbar\omega_{ac} = \Delta + Dq^2 \tag{3}$$

pictured in Figure 2.1, where Δ represents the spin wave gap and D is the acoustic spin-wave stiffness. This leads to the reduced spontaneous magnetization [16]

$$\frac{M_S(T)}{M_S(0)} = 1 - \frac{1}{NS}\left(\frac{k_B T}{4\pi D}\right)^{3/2} \cdot \zeta\left(\frac{3}{2}, \frac{\Delta}{k_B T}\right) \tag{4}$$

where $M_S(T)$ is the spontaneous magnetization at temperature T and ζ is the modified Riemann-zeta function

$$\zeta(\alpha, \beta) = \sum_{p=1}^{\infty} \frac{\exp(-p \cdot \beta)}{p^{\alpha}},$$

N is the number of Mn sites per unit volume and S is the spin. A schematic representation of the reduced spontaneous magnetization is shown in Figure 2.2.

2.3 Arrott-Noakes Equation of State: Estimates for the Spontaneous Magnetization

Following the thermodynamic approach of Landau and Lifshitz [17], it's possible to show that near the ferromagnetic transition it is possible to write the free energy in terms of a power series expansion of the reduced magnetization m, where $m = M_S(T)/M_S(0)$ such that

$$f(m, T) = f_0(T) + c_1(T)m + c_2(T)m^2 + c_3(T)m^3 + c_4(T)m^4 + \ldots \tag{5}$$

near the transition temperature (T_C), where $m \ll 1$. Symmetry shows that the odd term parameters should be zero, since a reversal of magnetization should not affect

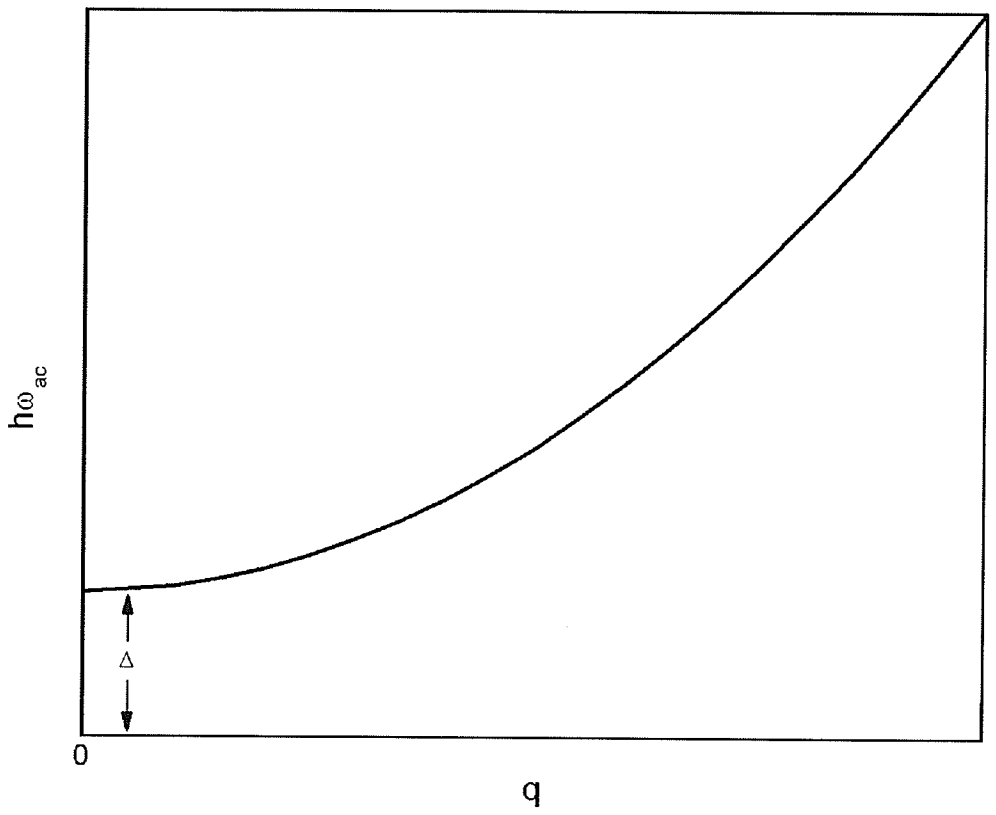

Figure 2.1: *Schematic diagram showing the gapped dispersion relation, Eq.* (3).

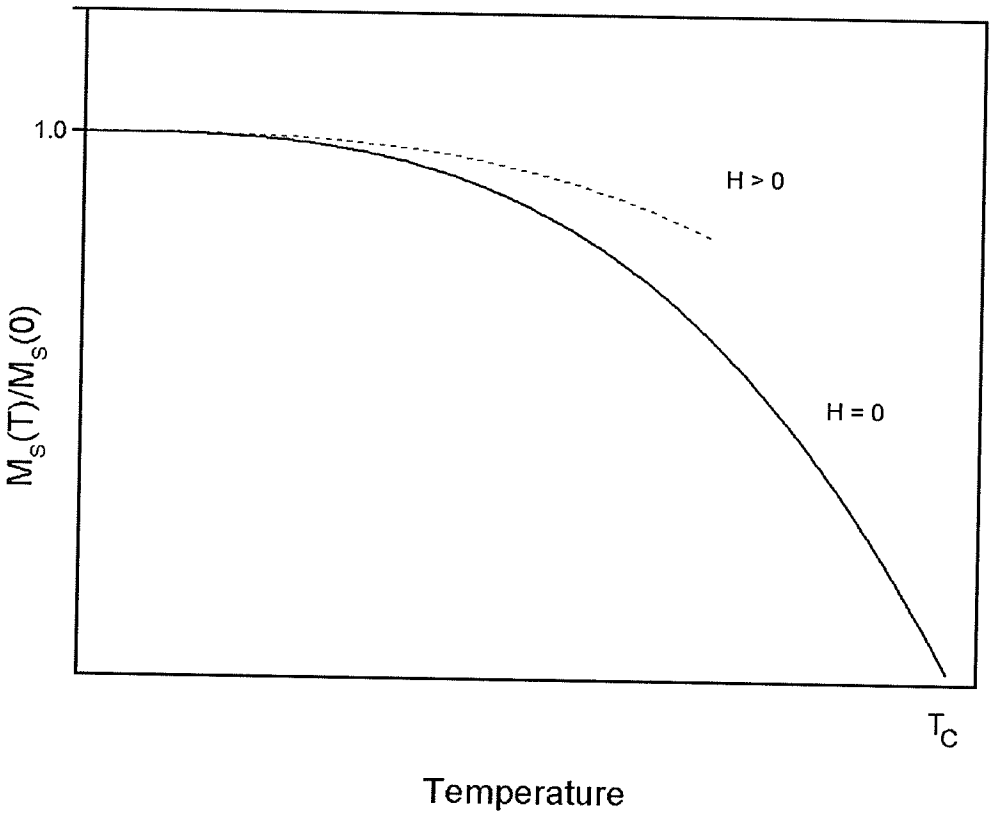

Figure 2.2: *Demonstration of the typical behaviour of the reduced spontaneous magnetization. The solid line shows the behaviour following the common $T^{3/2}$ fit in the absence of a field, while the dashed line represents the "flattening" effect a magnetic field has.*

the free energy in systems with inversion symmetry. $c_2(T)$ is chosen such that the minimum of $f(T,m)$ will correspond to $m = 0$ for temperatures $T > T_C$ and is given the simplest form $c_2(T) = c_0(T - T_C)$ with $c_0 > 0$. In order for equilibrium and stability to exist, $\left(\frac{\partial F}{\partial m}\Big|_T = 0\right)$ and $\left(\frac{\partial^2 F}{\partial m^2}\Big|_T > 0\right)$ must be true.

This condition gives $c_4 > 0$. The presence of an external field H, adds the term -mH to Eq. (5). The equilibrium condition then yields

$$\left.\frac{\partial F}{\partial m}\right|_T = c_0(T - T_C)m + c_4 m^3 - H = 0,$$

which, once rearranged, gives the modified Arrott plot

$$\frac{H}{m} = c_0'(T - T_C) + \frac{m^2}{c'},$$

which is equivalent to the Arrott-Noakes equation of state

$$\left(\frac{H}{M}\right)^{1/\gamma} = \left(\frac{M}{M_1}\right)^{1/\beta} + \left(\frac{T - T_C}{T_C}\right) \tag{6}$$

where M_1 is a material constant, using mean-field parameters ($\gamma = 1$, $\beta = 1/2$). The Arrott plot pictured below details the usefulness of this technique. Data that extends through the origin give the value of T_C while data intersecting the y-axis give the spontaneous magnetization and data intersecting the x-axis give the inverse of the initial susceptibility.

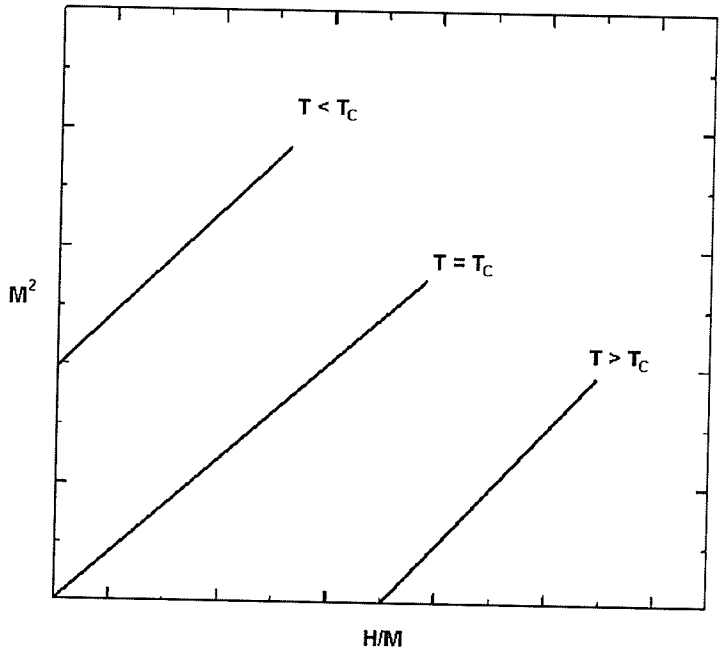

Figure 2.3: *Examples of Arrott plots, highlighting the properties attained.*

2.4 Coercivity

Another property exhibited by ferromagnets is hysteresis, a non-single valued relationship between magnetization and field in a material, pictured below. From the hysteresis curve, coercivity is defined as the field necessary to reduce the magnetization to zero.

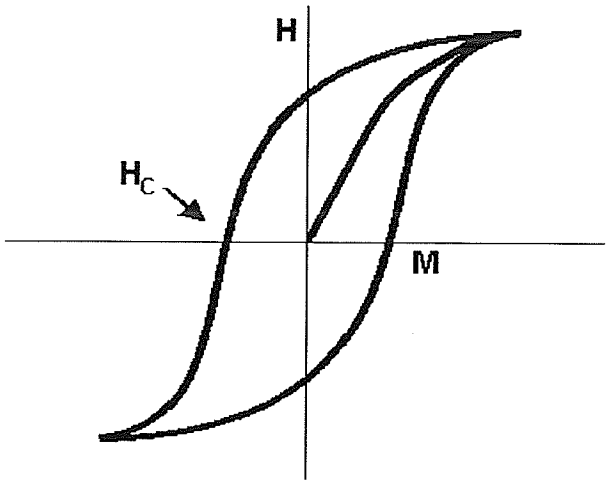

Figure 2.4: *Plot of magnetization versus magnetic field demonstrating the hysteretic property of ferromagnets.*

The replacement of La with the divalent R in manganese perovskites converts a percentage of the Mn ions from Mn^{3+} to Mn^{4+} as discussed previously. Mn^{3+} ($t_{2g}^3 e_g^1$, $S = 2$) is a "Jahn-Teller" ion which exhibits spin-orbit coupling, while Mn^{4+} (t_{2g}^3, $S = 3/2$) has no such coupling. This spin-orbit coupling is a mechanism which is capable of initiating coercivity in low fields [18].

In $La_{1-x}R_xCoO_3$, a material also studied in this thesis, the La replacement by the divalent R converts a number of Co ions from Co^{3+} to Co^{4+} for the same reason as in the manganite case. $Co^{3+}(t_{2g}^6,\ S = 0)$ does not have any spin orbit coupling, but Co^{4+} (t_{2g}^5, $S = 1/2$) or ($t_{2g}^4 e_g^1$, $S = 3/2$) does experience the coupling. Therefore the Co^{4+} could provide a mechanism for coercivity at low fields.

2.5 Magnetic Saturation

As the magnetic field is increased, the magnetization of a ferromagnetic material increases. A point is reached when the magnetization can no longer increase as all

the spins are aligned. This is the saturation magnetization and for a system of N atoms carrying spin S, the magnetic moment is given by $g\mu_B S$, where g is the Lande g factor, and the saturation magnetization is given by $Ng\mu_B S$.

2.5.1 Approach to Saturation

The experimental form adopted to describe the approach to saturation of a ferromagnetic material is given by [19, 20]

$$M_H(T,H) = M_{SAT}(T) - \frac{a(T)}{H} - \frac{b(T)}{H^2} + \chi(T)\cdot H. \tag{7}$$

$M_H(T,H)$ is the measured magnetization along the direction of the field, $M_{SAT}(T)$ is the saturation magnetization at temperature T. The form actually constitutes a power series in the inverse field (H^{-1}) in which only the first few terms are retained [19]. The $\frac{a(T)}{H}$ term is generally attributed to the effect of crystal imperfections in the material such as stress fields about dislocations [18] and non-magnetic inclusions [22]. The $\frac{b(T)}{H^2}$ term is a restoring force which reflects the opposing torques caused by applied field and the crystalline anisotropy.

$$b(T) = \frac{\alpha K(T)^2}{M_{SAT}(T)} \tag{8}$$

where α is a geometric constant (see Appendix A for the calculation of b(T) and α) and $K(T)$ is the anisotropy constant which is characteristic of a given material and is temperature dependent [23].

The $\chi(T)\cdot H$ term represents an increase in the spontaneous magnetization of a domain caused by an increased external magnetic field [18], likely due to a redistribution of population of spin states induced by the field.

Eq. (7) is the form adopted to discuss the approach to saturation in Chapter 5, and deduce the corresponding anisotropy constant $K(T)$.

Chapter Three

3 The $LaBaMnO_3$ System

Transition metal oxides have been studied for many years. As mentioned in [1], much of the work has been focused on systems with Sr and Ca doping with less attention focused on Ba doping. Below, some important information on current work on the $LaBaMnO_3$ system is summarized as it relates to specific topics outlined in previous chapters.

3.1 Neutron Scattering

3.1.1 Gap Parameters

A single crystal sample of $La_{0.7}Ba_{0.3}MnO_3$ was investigated at temperatures ranging from 1.5-349 K using inelastic neutron-scattering by Chatterji et al [24] which confirmed the applicability of acoustic spin wave theory to low-lying magnetic excitations well below T_C. They measured a gap parameter $\Delta = 0.20 \pm 0.04\ meV$ with $D = 152 \pm 3\ meV$ Å^2.

3.1.2 Structural Phase Change

Chatterji et al. also measured a structural phase change from a high temperature rhombohedral R3c phase to lower temperature orthorhombic Pbnm/Imma phase, in their sample at $T = 180\ K$.

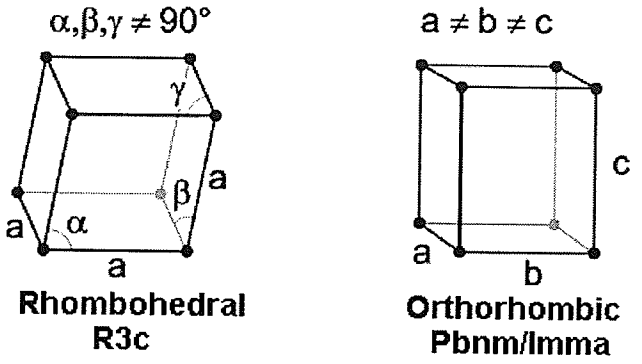

Figure 3.1: *Diagram of the rhombohedral R3c phase and the orthorhombic Pbnm/Imma phase.*

Similar phase changes have also been measured in samples with $x = 0.2$ [25, 26] and $x = 0.33$ [27]. These phase changes again occurred approximately around $T = 180\ K$. These changes are thought to be reflected in an increase in the resistivity at this temperature; resistivity data from Laukhin et al [25] are shown below, where the presence of hysteretic behaviour is also highlighted.

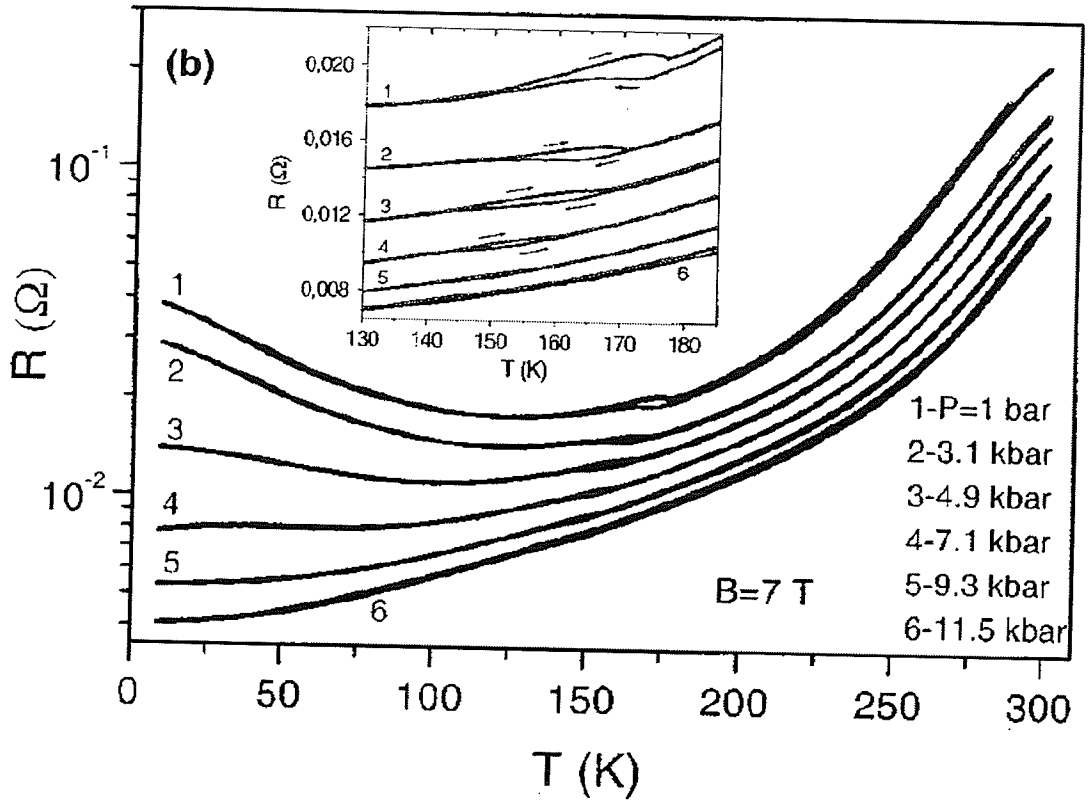

Figure 3.2: *Data from Laukhin et al. [25] showing evidence of a phase change around 180 K, visible by a rise in resistivity. The inset shows evidence of hysteresis in the sample.*

3.2 AC Susceptibility

The phase change seen in the resistivity data is also visible as a decline in the ac susceptibility, $\chi_{ac}(0,T)$ occurring near the same temperature. An example of this decline in χ_{ac} is shown below in data from Laukhin et al [25].

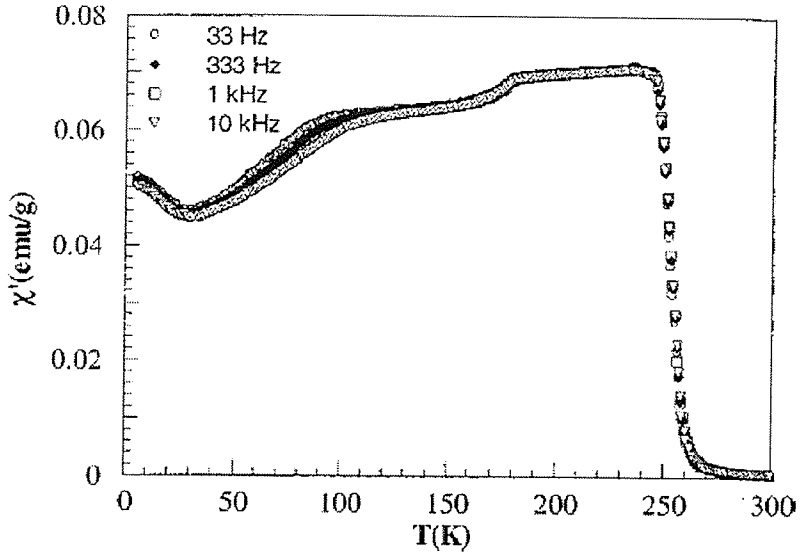

Figure 3.3: *The phase change mentioned in Figure 3.2 is also visible as a decrease in χ_{ac} also occurring around 180 K.*

χ_{ac} measurements made on an $x = 0.2$ sample showed a two step decrease at temperatures around 200 K and 100 K as shown above. Laukhin et al [25] discussed the drop in χ_{ac} near 200 K in terms of the structured phase change mentioned earlier, but not the second drop near 100 K. If this latter drop were the result of an applied field, the field induced suppression might be identified with domain wall pinning. One would expect a frequency dependence along with this, while such a dependence is clearly not present in the data shown above.

3.3 Thermal Expansion

Measurements made on the thermal expansion of samples with $x = 0.2$ [28] and $x = 0.3$ [29] provide further evidence of the structural phase change occurring in this system. The lower composition has a definite anomaly around $T = 175\ K$, identified with the R3c to Pbnm/Imma phase change seen in neutron scattering. As shown in the two figures below, this anomaly is barely visible in the higher composition sample.

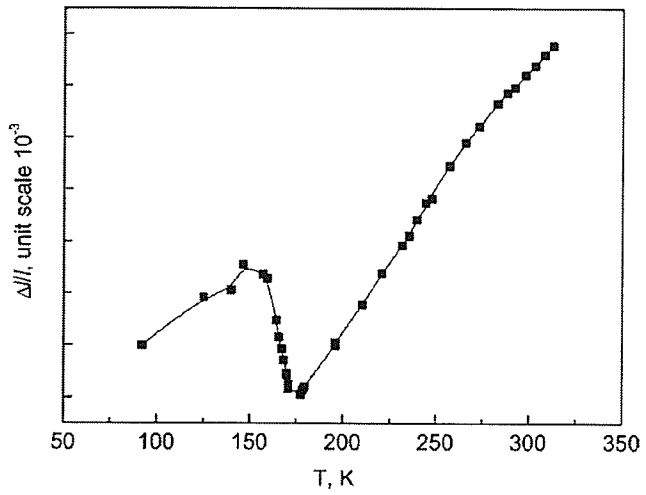

Figure 3.4: *Data from Demin et al. [28] showing the phase change from R3c to Pbnm/Imma occurring at 175 K in the $x = 0.2$ sample.*

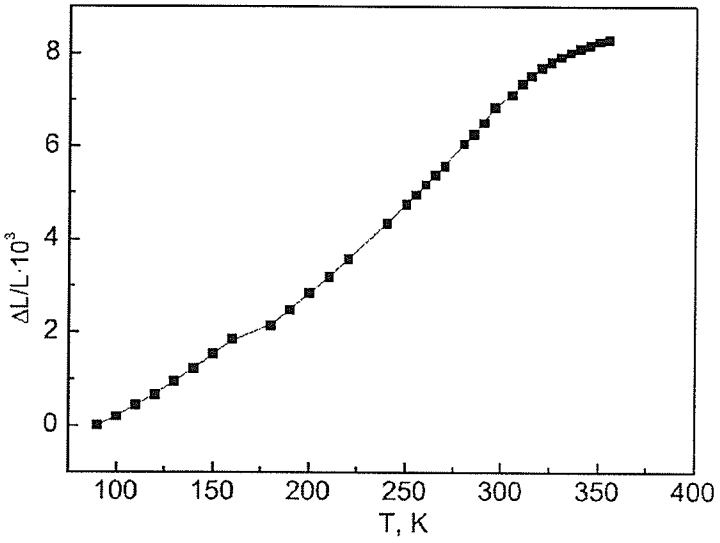

Figure 3.5: *The phase change seen in Figure 3.4 is barely visible in the $x = 0.3$ sample.*

Chapter Four

4 Experimental Details

To study both the approach to saturation and the spontaneous magnetization, measurements of DC magnetization were carried out on a sample composed of $La_{0.73}Ba_{0.27}MnO_3$. DC magnetization measurements were also made on a sample of $La_{0.5}Sr_{0.5}CoO_3$ for comparison. The manner in which the samples were prepared along with details of the apparatus are outlined in this chapter.

4.1 Sample Preparation

4.1.1 Single Crystal $La_{0.73}Ba_{0.27}MnO_3$

The sample used in the following experiments was a single crystal $La_{0.73}Ba_{0.27}MnO_3$ obtained from collaborators at the Moscow State Steel and Alloys Institute. The sample was made using a floating zone technique described below, resulting in high structural and magnetic quality. Mosaicity, a measurement of structural deviation from that of a perfect crystal, was less than 1°. The measured coercive field was less than 10 Oe . A summary of the properties of this sample is given below.

Table 4.1 Sample Description

$La_{0.73}Ba_{0.27}MnO_3$	
Mass [g]	0.163
Length [mm]	6
Average Radius [mm]	1.6
Density $\left[\frac{g}{cm^3}\right]$	6.76

4.1.2 Floating Zone Technique

First demonstrated by Keck and Golay [30], the floating zone technique has become the standard for producing high quality, single crystal oxides. Using this technique it is possible to recreate the atmospheres and pressures under which a crystal would naturally form.

A high quality polycrystalline *feed rod* and a single crystal *seed rod* of the desired composition are placed vertically within a sealed quartz chamber. It is within this chamber that the pressure and atmosphere can be controlled. The end of the feed rod is heated to melting. Surface tension causes the molten material to *float* between the feed and seed rods. Different heating techniques are used, from halogen bulb with elliptical mirrors used for focusing as shown in Figure 4.1, to laser light. Once the *float zone* of molten material has stabilized in the region between the feed and seed rods they are lowered at rates of millimetres/hour allowing crystal layer growth at the boundary between the molten float and the seed rod. These new layers grow with the same symmetry as the seed rod. To encourage uniform mixing and an even heat distribution, the rods are rotated opposingly. Depending on the desired rate of growth, the entire process can take from hours to days. Often multiple single crystals are formed along the length of the seed rod; it is necessary that they be cut into multiple single crystals.

4.1.3 Polycrystalline $La_{0.5}Sr_{0.5}CoO_3$

A second sample used for comparison was obtained from Senchuck et al. [31]. Stoichiometric quantities of La_2O_3, $SrCO_3$ and Co_3O_4 were combined and ground in a ball mill with acetone for twenty-four hours. After being dried and shaped into pellet form, the sample was fired at 900 $^\circ C$ for another twenty-four hours.

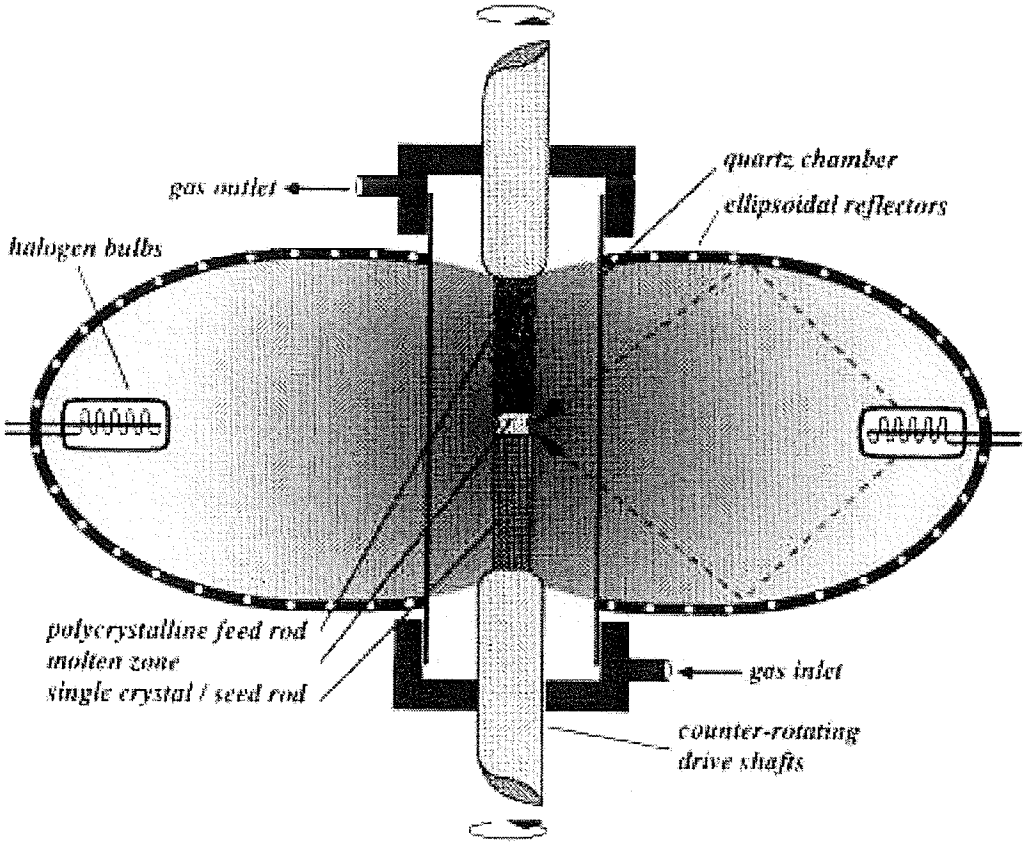

Figure 4.1: *Schematic diagram of the floating zone technique using halogen heat sources.*

The sample was reground and then fired in flowing oxygen for twenty-four hours at 1000 $^{\circ}C$ and ninety-six hours at 1050 $^{\circ}C$. Powder X-ray diffraction showed the sample to be of a single phase and it was indexed as a pseudo-cubic perovskite-like cell. A summary of the properties of this sample is given below.

Table 4.2 Sample Properties

$La_{0.5}Sr_{0.5}CoO_3$	
Dimensions $[mm^3]$	6 x 1 x 1
Density $\left[\frac{g}{cm^3}\right]$	6.4675
Lattice Constant [Å]	3.838

4.2 Experimental Apparatus

A Quantum Design PPMS model 6000 magnetometer with an ACMS probe was used to make all measurements on the above samples. A brief description of the magnetometer follows.

4.2.1 PPMS Magnetometer

The PPMS magnetometer, pictured in Figure 4.2, allows automated measurement on the magnetic properties of materials to be carried out, including AC susceptibility, DC magnetization, at various temperatures. The magnetometer is capable of producing fields to 9 T and temperatures from 2-350 K. A schematic diagram of the PPMS probe is shown in Figure 4.3.

Temperature Control

For temperature control above the boiling point of liquid helium (4.2 K) a block heater is used to warm the sample. A second heater above the sample is also used in order to reduce thermal gradients within the sample area.

Figure 4.2: *Picture of PPMS. This and the following two diagrams are taken from the Quantum Design brochure.*

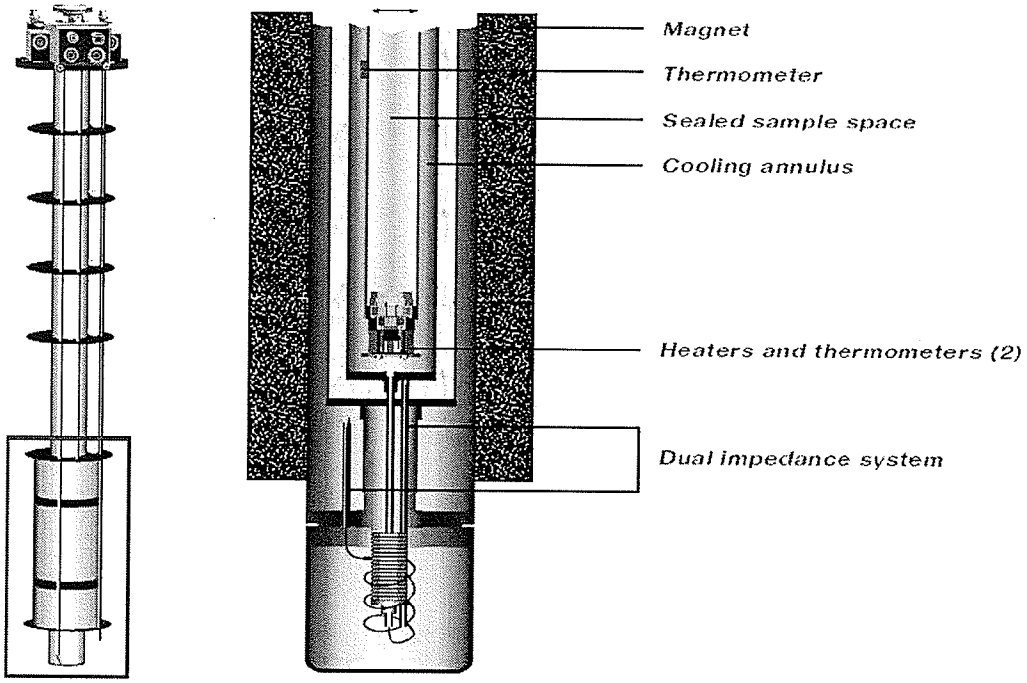

Figure 4.3: *Diagram of PPMS probe*

Helium vapour within the sample area is also heated by the block heater, which allows for more uniform heating of the sample. Helium vapour is drawn across the sample in order to cool it. In the following experiments a heating/cooling rate of 20 K/min was used.

To reach temperatures below 4.2 K, the cooling annulus is partially filled with liquid helium. Altering the atmospheric pressure of the annulus results in the boiling point of the helium being changed. Lowering the pressure causes the liquid helium to boil at a lower temperature resulting in low temperature helium vapour filling the sample area and cooling the sample. Temperatures of approximately 1.8 K can be reached by use of this technique. Warming of the sample in this temperature regime is controlled by raising the atmospheric pressure in the cooling annulus.

The PPMS uses two different approach modes to alter the samples temperature. When set to the *fast settle* mode the temperature is cooled(raised) below(above) the desired temperature and then allowed to heat (cool) up (down) to the desired temperature. When in the *no overshoot* mode the desired temperature is approached slowly, from one direction. This mode takes longer, but no overshoot of the selected temperature occurs, which can be important when measuring temperature related properties.

The temperature of the sample is measured by two separate thermometers mounted at the bottom of the sample space. A platinum resistance thermometer is used for measurements above 80 K, while a negative temperature coefficient (NTC) thermometer is used for temperatures less than 100 K. For temperatures in the overlap range of 80 - 100 K, a weighted average from the two thermometers is used.

Magnetic Field Control

The PPMS magnetometer uses a superconducting Niobium/Titanium alloy solenoid to provide a uniform magnetic field across the sample with a field homogeneity of 0.01% within the sample space. The current through the magnet is controlled in the following way. The magnetic power supply matches the current present within the magnet. A superconducting *persistence switch* is heated to a temperature such that it is no longer able to superconduct thus allowing the power supply to become part of the magnet circuit. Using a device-specific field to current ratio the magnetic power supply changes the current to the level required for the desired field strength. The persistence switch is then allowed to cool, regaining superconductivity thus completing the superconducting circuit. This is referred to as the *persistence mode* of the magnet. The magnet can also be set to be directly controlled by the the power supply. In this *driven mode* the connection between the magnet and the power supply is maintained which allows for faster changes in the magnetic field but the resulting signal is much nosier than that obtained in persistence mode and an increased amount of liquid helium is boiled off.

To control the magnetic field, three different approach modes may be utilized. In the *oscillate mode* the magnetic field oscillates in decreasing steps above and below the set field until the desired strength is obtained. Samples that exhibit hysteresis may be adversely affected by the oscillation around desired field strength. To avoid this problem the *no overshoot* mode can be employed. The field is increased in steps in decreasing steps from one direction until the desired strength is obtained. Both of the previous modes require considerably more time than the *linear mode*. The PPMS attempts to charge directly to the desired field strength, and then fine tunes to get it right. This mode is the fastest, but can result in both magnetic relaxation and overshooting.

For fields above 9000 Oe, the PPMS won't make measurements until the field is within 1 Oe of the set strength. For lower fields, the tolerance is around 0.1 Oe. The PPMS does not account for remnant fields within the magnet itself. Ideally there should be none, but for the device used in these experiments, a remnant field of typically 10-25 Oe was observed. To account for this field, the set values were scaled back by the observed remnant field.

Helium Level

Liquid helium is vitally important for the proper performance of the PPMS. Running measurements without the proper amount can result in permanent damage to the magnet. The level of the helium is monitored by a superconducting rod that runs the length of the probe. When the rod is not immersed in liquid helium it becomes non-superconducting and a resistance is measured. This resistance is compared with a calibration value and thus the helium level can be monitored.

4.2.2 ACMS Probe

DC magnetization of the sample is measured using the ACMS probe shown in Figure 4.4.

Detection Coils

The probe uses a detection coil made of two sets of counter wound copper coils connected in series. The arrangement of the coils is configured to isolate the sample signal from any background sources.

DC Magnetization Measurements

The sample was placed at the end of a *sample rod* which is moved within the probe by the *transport assembly*. The temperature and magnetic field within the sample space are both controlled by the magnetometer. A constant field is applied to the sample by the PPMS, and the sample is moved quickly through the detection coils. The motion of the sample induces a voltage in the coils proportional to rate of change of magnetic flux translating through them. The ACMS takes 4096 readings of these voltages and creates a voltage profile curve. The curve is numerically integrated and fitted to the known waveform of a dipole moving through the detection coils. The transport assembly can translate the sample through the coils in 0.05 seconds allowing for the averaging of several scans thus reducing the error contributions to the reported result.

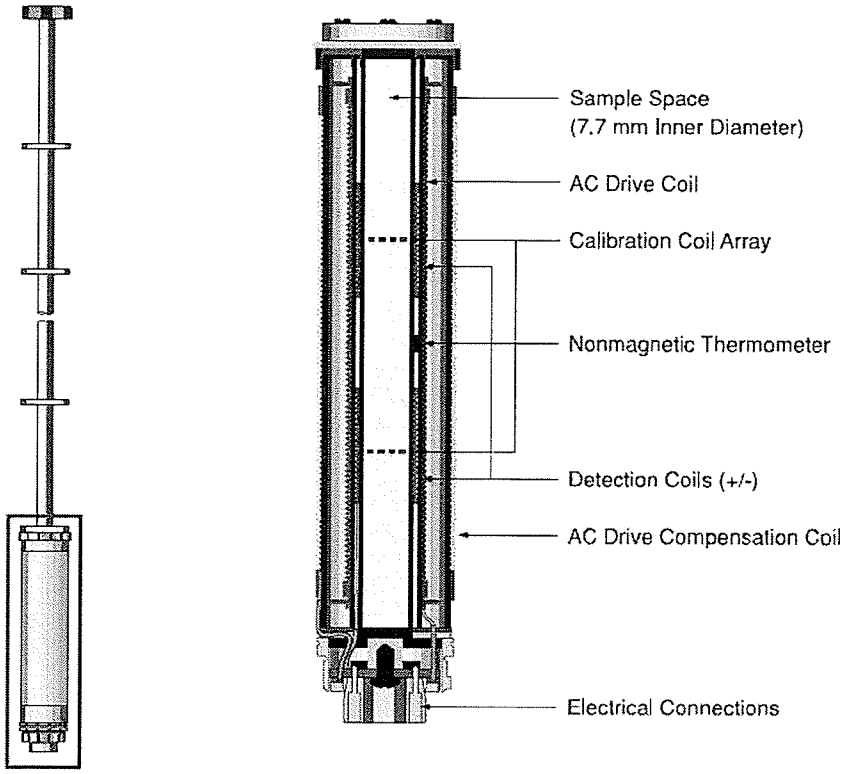

Figure 4.4: *Diagram of ACMS*

Chapter Five

5 Experimental Data

5.1 Data for $La_{0.73}Ba_{0.27}MnO_3$

5.1.1 Data Acquisition

Using a programmed sequence, measurements on the sample were made by the Quantum Design PPMS magnetometer with ACMS probe. The temperature of the sample was raised to 300 K, well above the Curie temperature ($T_C = 245.0\ K$ [32]), in zero field to demagnetise the sample. The temperature was then lowered to a predetermined value and held for five minutes to ensure thermal equilibrium. Measurements at temperatures from 2-250 K were carried out on this sample in this manner. After the five minute wait, the sample was measured in field strengths from 0-80000 Oe using the magnetometer set in persistent mode with no-overshoot. The magnet was then set to zero and the temperature raised above T_C before taking the next measurement by repeating the above procedure. The acquired data are shown in Figure 5.1.

5.1.2 Spontaneous Magnetization

The spontaneous magnetization was found using conventional extrapolations from the Arrott-Noakes equation of state, Eq. (6)

$$\left(\frac{H}{M}\right)^{1/\gamma} = \left(\frac{T - T_C}{T_C}\right) + \left(\frac{M}{M_1}\right)^{1/\beta}$$

as discussed in Chapter 2.

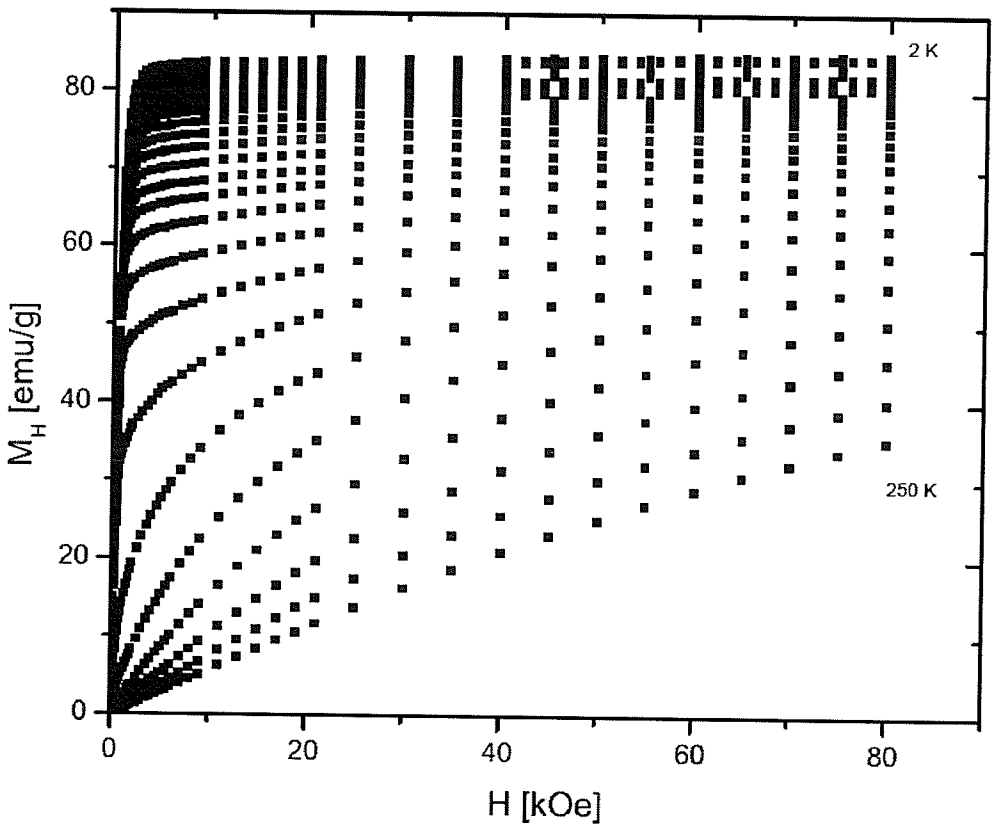

Figure 5.1: *Magnetization versus Temperature for* $La_{0.73}Ba_{0.27}MnO_3$. *Higher temperatures have a lower magnetization than lower temperatures. Temperatures shown range from 2-44 K (highest data) in 2 K steps, 45-80 K in 5 K steps and 90-250 K (lowest data) in 10 K steps.*

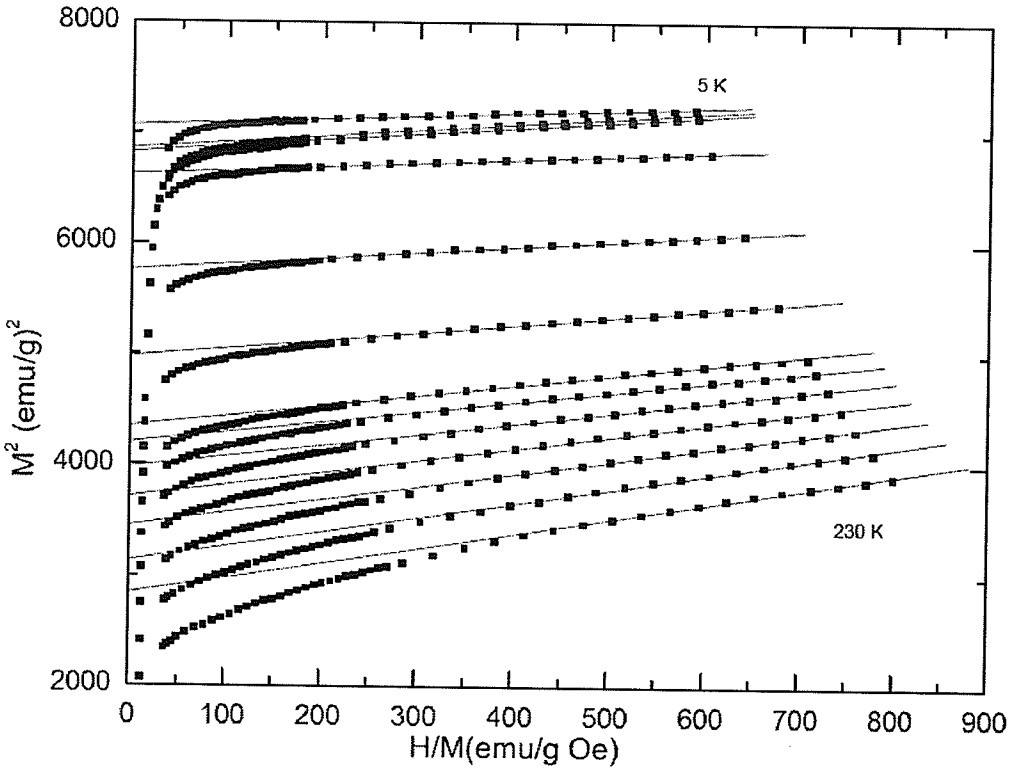

Figure 5.2: *Arrott-Noakes plots for the following temperatures using mean field exponent values. Temperature values are 5 (top), 25, 100, 150, 180 K and 200-230 K in 5 K steps.*

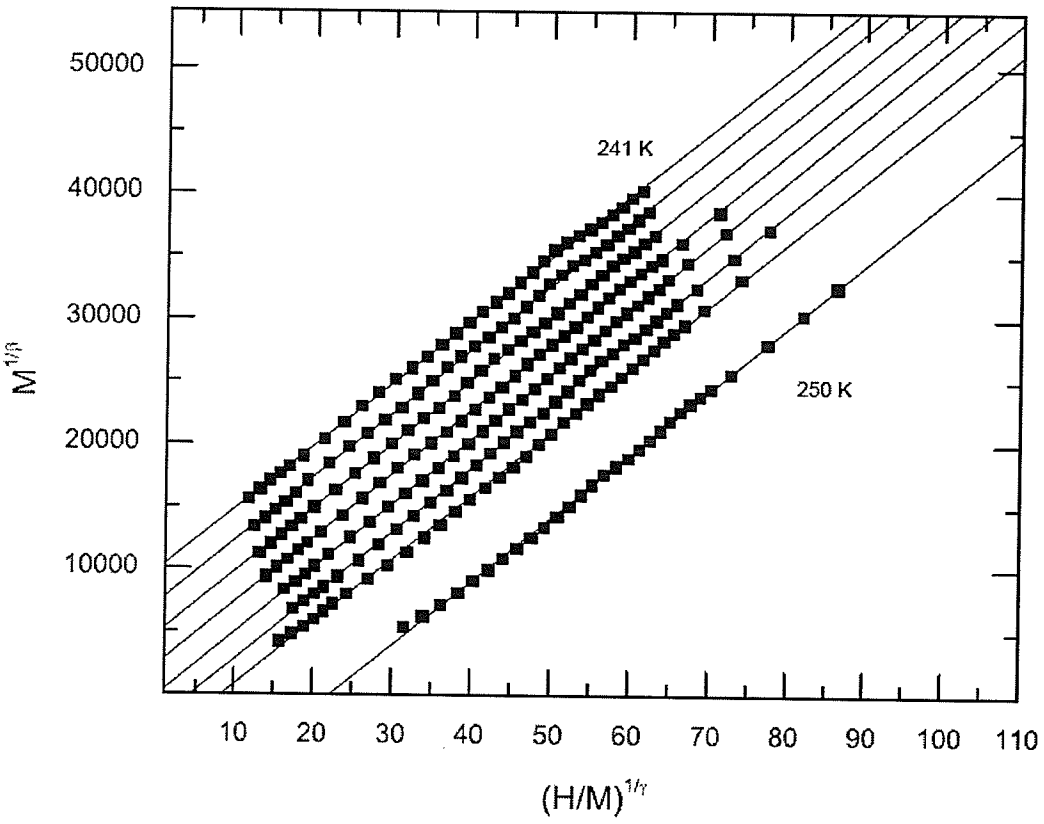

Figure 5.3: *Arrott-Noakes plots for temperatures near T_C using the Heisenberg model exponents ($\gamma = 1.386$, $\beta = 0.364$). Temperatures range from 241-247 K (top) in 1 K steps. 250 K (lowest data) is also shown. T_C is estimated as 245.0 K by extrapolating between the two isotherms passing closest to the origin.*

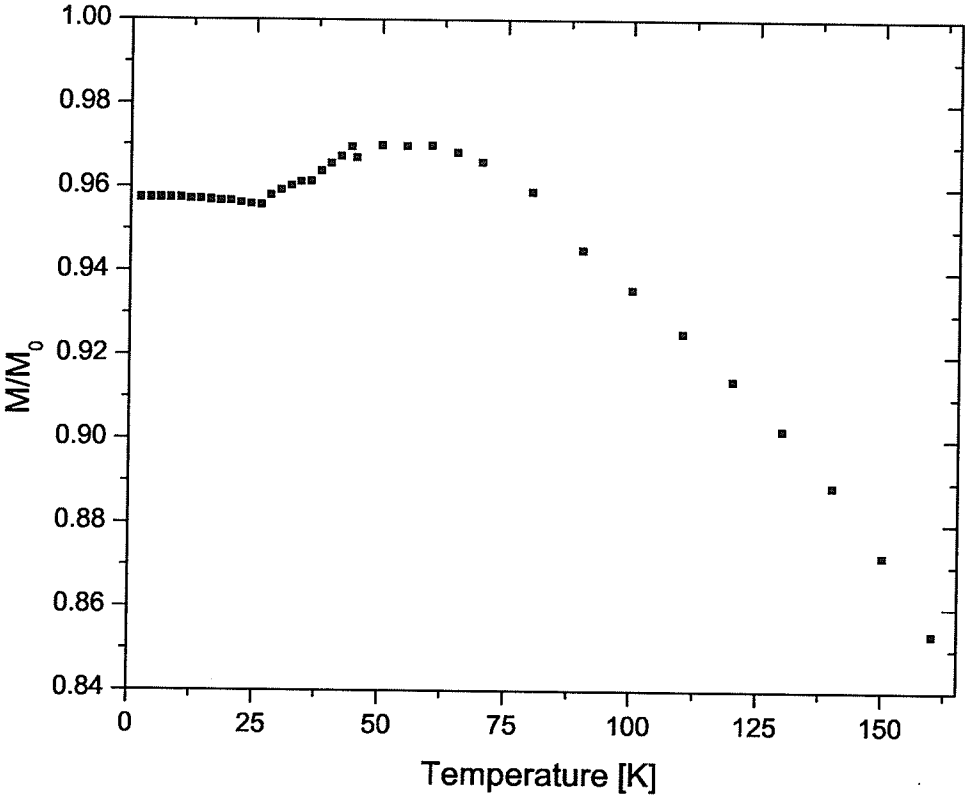

Figure 5.4: *Summary of the reduced spontaneous magnetization obtained from Arrott plots.*

In the temperature region below $\frac{T_C}{2}$, mean-field exponents are applicable and are shown in Figure 5.2, but for temperatures close to T_C it is necessary to use the Heisenberg-model values ($\gamma = 1.386$, $\beta = 0.364$) [32] shown in Figure 5.3. Figure 5.4 reproduces the temperature dependence of the reduced spontaneous magnetization $M_S(T)/M_S(0)$ taken from the intercepts in Figures 5.2 and 5.3. Analysis of this data is presented in later chapters.

5.1.3 Approach To Saturation

To fit data acquired, in essentially the opposite regime to that used to estimate the spontaneous magnetization, the approach of the magnetization to saturation was represented by Eq. (7)

$$M_H(T,H) = M_{SAT}(T) - \frac{a(T)}{H} - \frac{b(T)}{H^2} + \chi(T) \cdot H.$$

The first attempt at fitting was made by writing the function into the non-linear curve fitting program in Origin. As shown in Figure 5.5, this resulted in a good fit to the high field data, but the negative obtained value for b(T) causes a severe increase in the value at low fields illustrated in Figure 5.6. Comparing with Eq. (8), a negative b(T) is unphysical because $\frac{\alpha K(T)^2}{M_{SAT}(T)} \geq 0$.

An attempt to address this problem was made by obtaining a value for $M_{SAT}(T)$ from plots of $M_H(T,H)$ vs $\frac{1}{H}$ by extrapolation to $H^{-1} = 0$, shown in Figure 5.7. This value was then entered into Eq. (7) and kept fixed while a(T), b(T) and $\chi(T)$ were allowed to vary. As shown in Figure 5.8, a positive value for b(T) was now obtained, but a(T) was forced to become negative. As earlier discussed, a(T) is a value related to imperfections in the crystal and must also be positive.

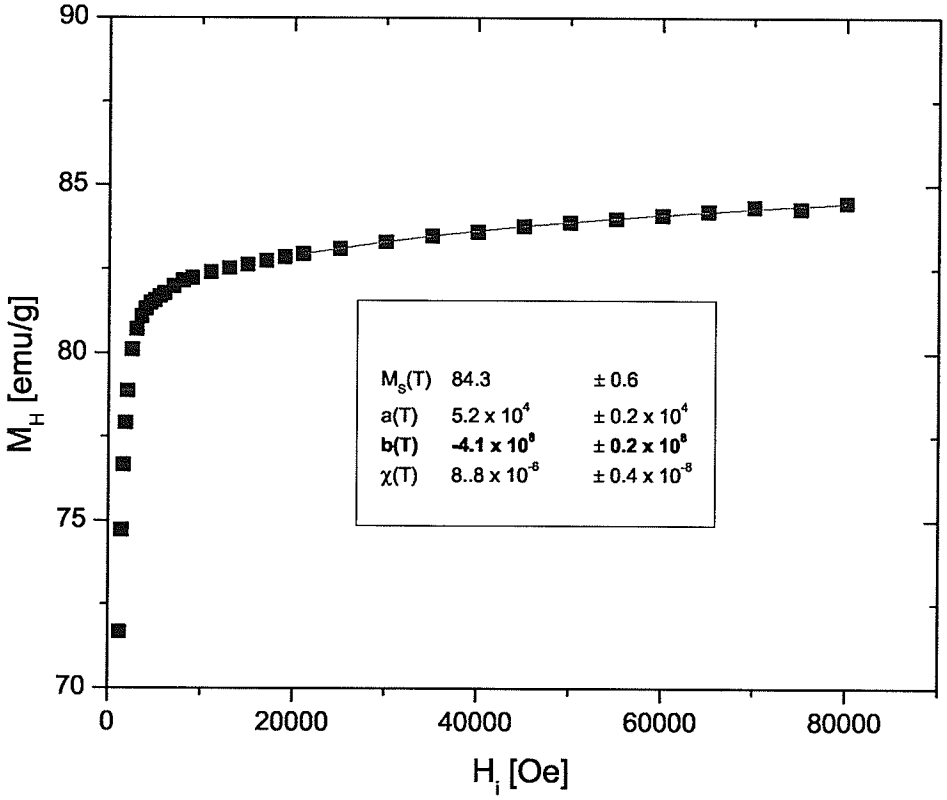

Figure 5.5: *Magnetization versus Temperature at 2 K fitted with* $M_H(T,H) = M_{SAT}(T) - \frac{a(T)}{H} - \frac{b(T)}{H^2} + \chi(T) \cdot H$. *The b(T) term is found to be negative.*

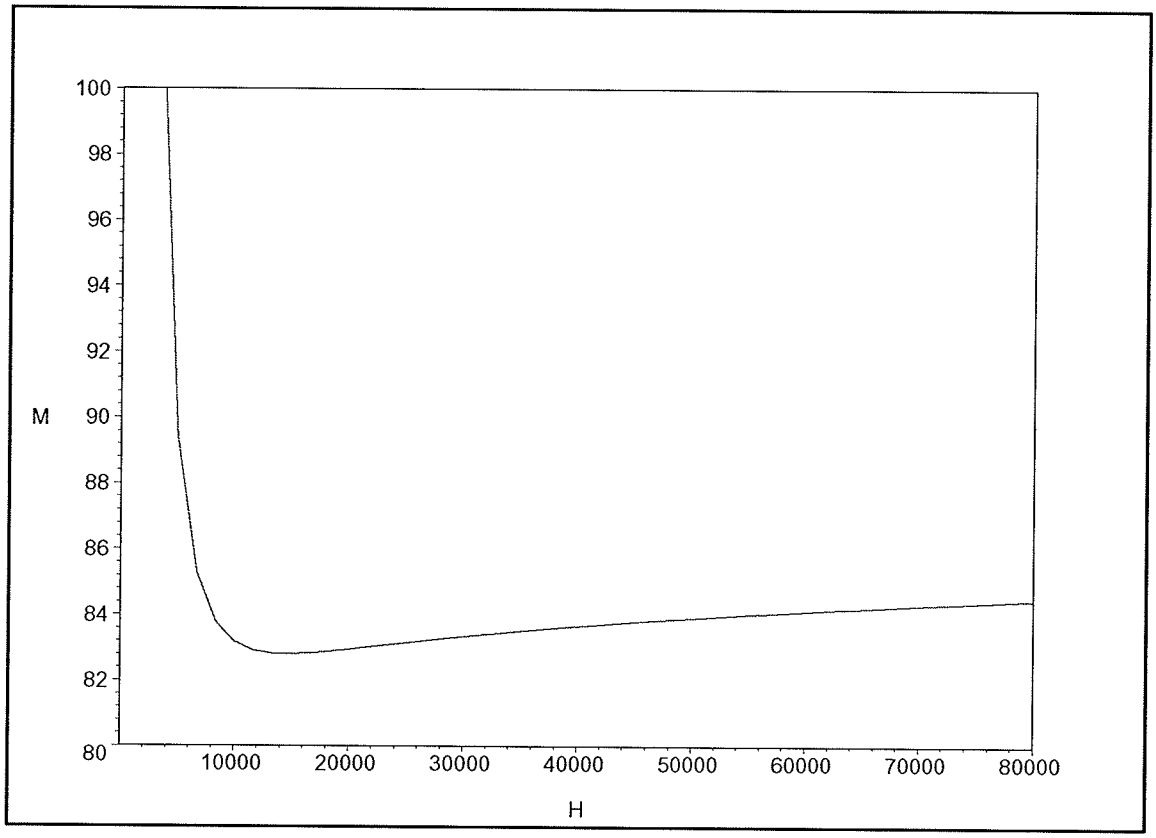

Figure 5.6: *Extrapolated values of the magnetization at low field using the previously fitted parameters. The negative b(T) term causes a sudden increase in magnetization at low H.*

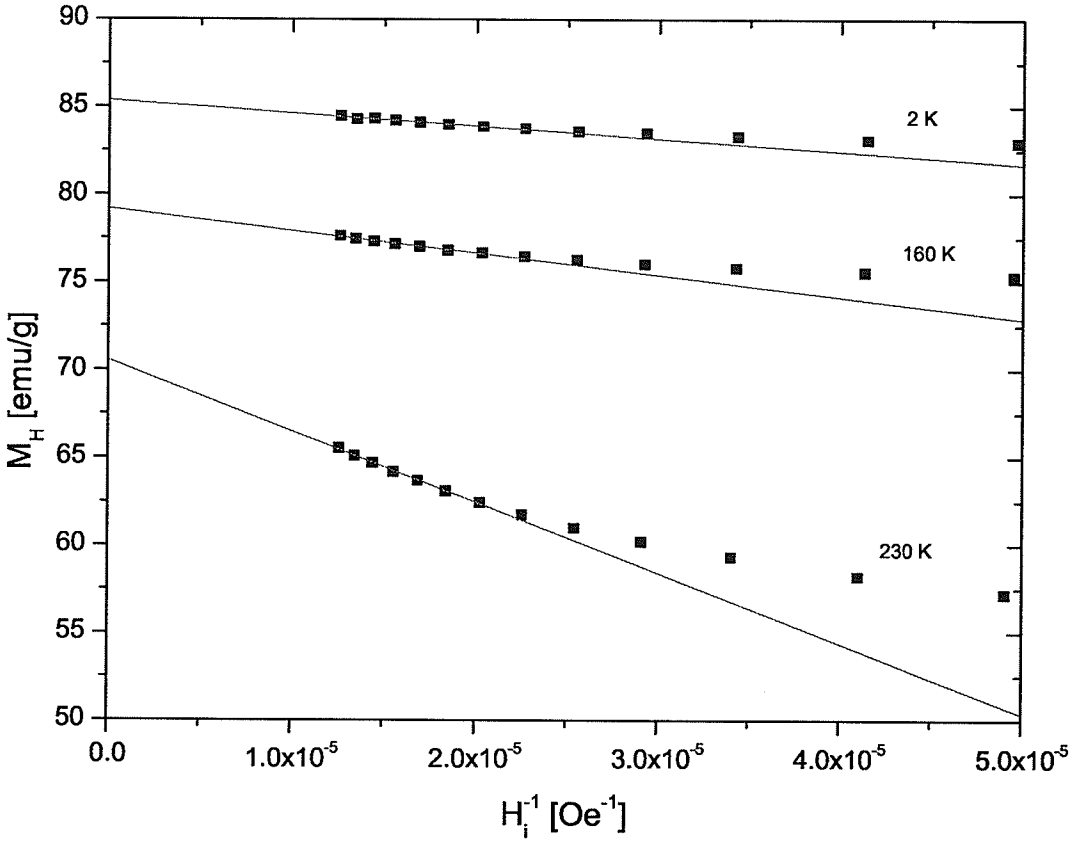

Figure 5.7: *Magnetization versus H^{-1} shown for 2, 160 and 230 K.*

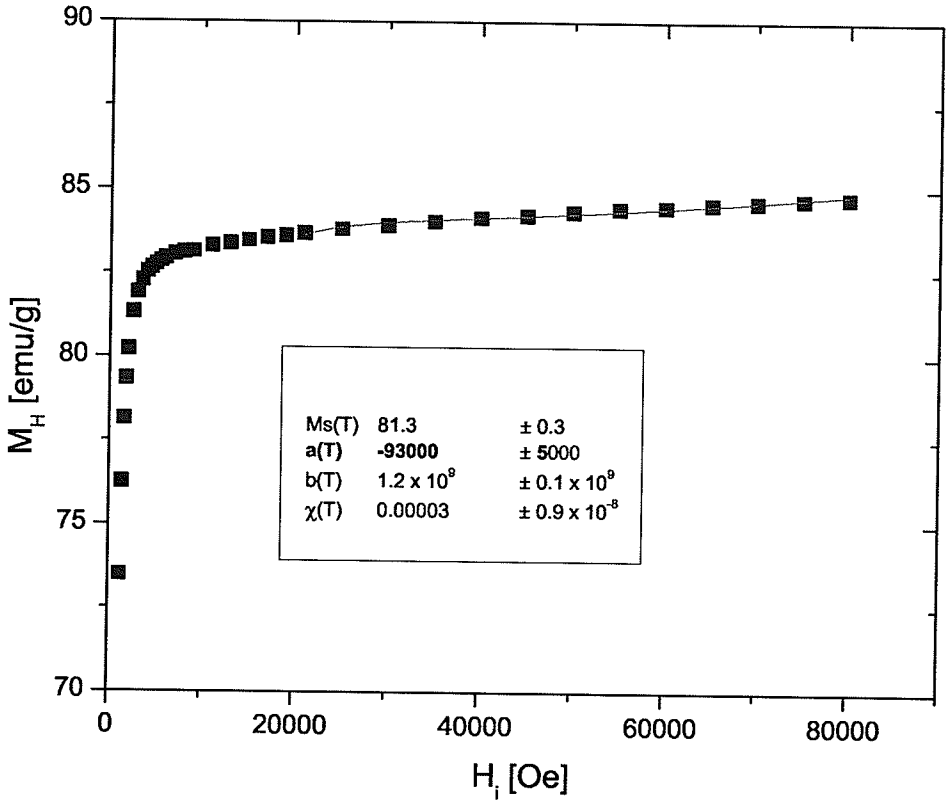

Figure 5.8: *Magnetization versus Temperature at 42 K fitted using* $M_H(T,H) = M_{SAT}(T) - \frac{a(T)}{H} - \frac{b(T)}{H^2} + \chi(T) \cdot H$ *with* $M_{SAT}(T)$ *being held at value determined from* M *versus* $\frac{1}{H}$ *plot. The* $a(T)$ *term has now become negative.*

Since it was not possible to consistently obtain positive values for both a(T) and b(T) an alternative method was followed. Because the sample being used was a single crystal of very high quality the role played by imperfections in the crystal, represented by a(T), should be minimal and thus it was set to zero.

A protocol for finding the values of $M_{SAT}(T)$, b(T) and $\chi(T)$ was developed. $\frac{b(T)}{H^2}$ is small within the high field regime (40-80 kOe), so the data were fit with a least squares fitting program shown in Figure 5.9, to obtain the values for $\chi(T)$ shown in Figure 5.10. The formula for approach to saturation can now be written as:

$$M_H(T,H) - \chi(T) \cdot H = M_{SAT}(T) - \frac{b(T)}{H^2}.$$

The slope of a least squares fit to $M_H(T,H) - \chi(T) \cdot H \; vs \; \frac{1}{H^2}$ shown in Figure 5.11, gives the values for b(T) shown in Figure 5.12.

Finally, the values for $M_{SAT}(T)$ shown in Figure 5.14, were obtained from the y-intercept of least squares fits to $M_H(T,H) - \chi(T) \cdot H \; vs \; \frac{1}{H}$ shown in Figure 5.13.

5.1.4 Magnetic Anisotropy

The magnetic anisotropy K(T) of the sample, shown in Figure 5.15, was found by rearrangement of Eq. (8), which gives

$$K(T) = \left(\frac{M_{SAT}(T) \cdot b(T)}{\alpha} \right)^{1/2}. \tag{9}$$

A value of $\alpha = \frac{8}{105}$ was used (see calculation in Appendix A). This value is acceptable for polycrystalline specimens exhibiting cubic symmetry [19, 20], but does not hold for a single crystal. Because the data is meant to be an approximation only, this value of α was used although it could be even lower for the single crystal, which would only serve to increase the discrepancy in K(T) discussed in Chapter 6.

The magnetic anisotropy constant $K(T)$ can also be found using

$$K(T) = \frac{H_C(T) \cdot M_{SAT}(0)}{A} \tag{10}$$

shown in Figure 5.16, where A is constant with value $0.1 \leq A \leq 1$ [20]. For the current analysis, A was set to 0.1 to obtain the maximum value for $K(T)$. The coercive field data in Figure 5.17 was obtained from Senchuk et al. [31] The saturation magnetization is given by $M_{SAT}(0) = 85.36\ emu/g$. This value was found from a plot at 2 K of $M\ vs\ H^{-1}$ shown in Figure 5.18.

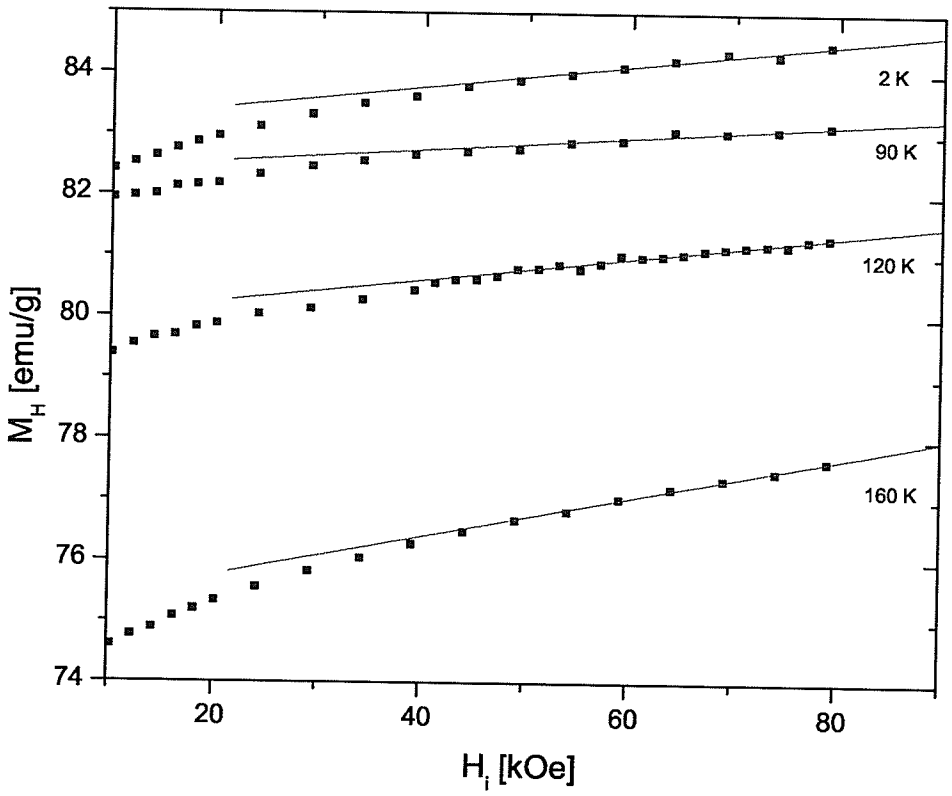

Figure 5.9: *High field magnetization versus temperature data linearly fitted to obtain a value for $\chi(T)$. Data for 2, 90, 120 and 160 K are shown.*

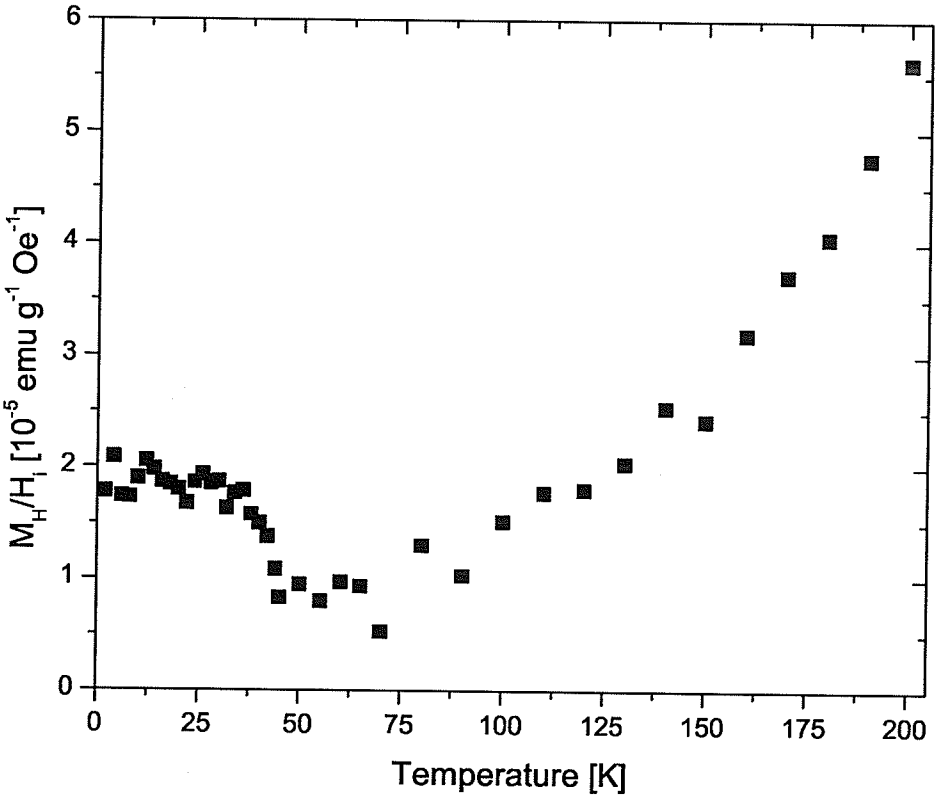

Figure 5.10: *Summary of* $\chi(T)$ *estimates.*

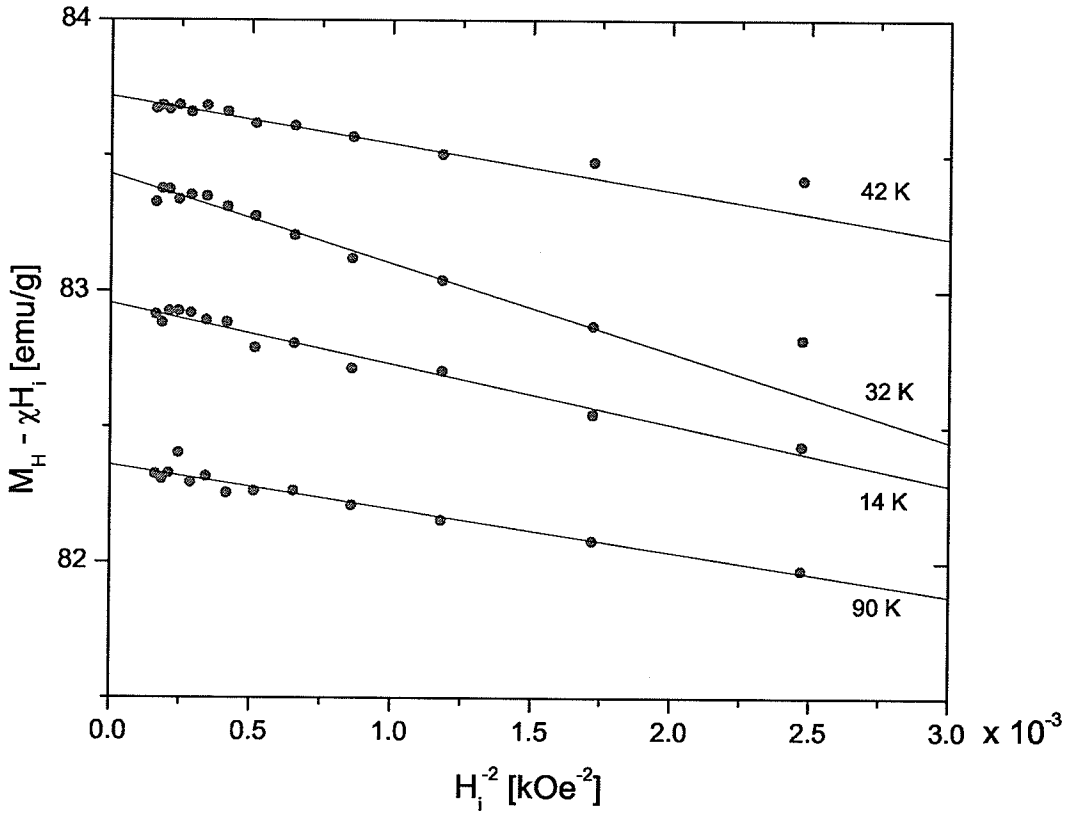

Figure 5.11: *Linear fit of high field data of* $M - \chi(T) \cdot H$ *versus* H^{-2} *gives a value for b(T). Data for 14, 32, 42 and 90 K are shown.*

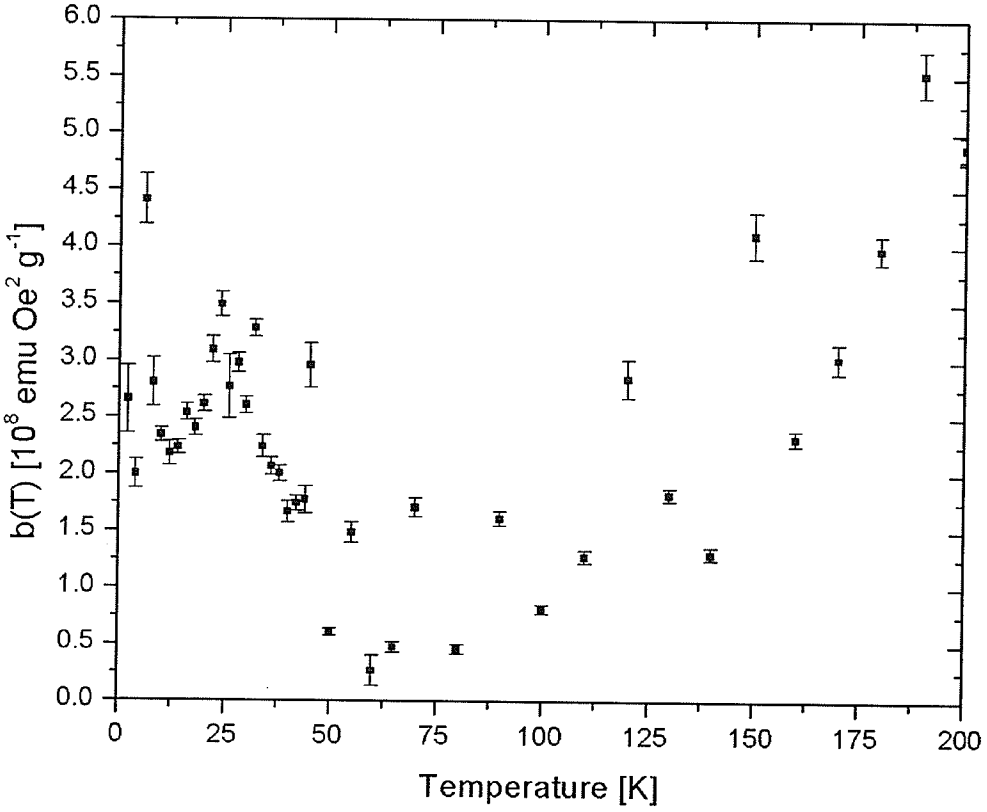

Figure 5.12: *Summary of b(T) values.*

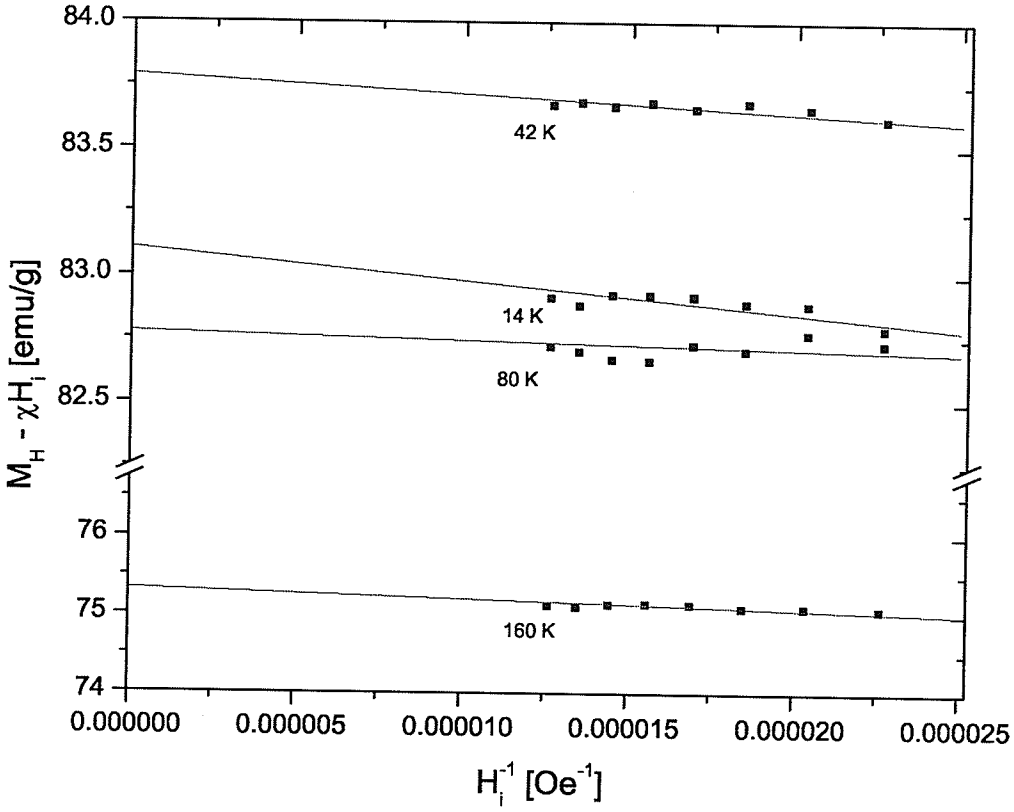

Figure 5.13: *Y-intercept of* $M - \chi \cdot H$ *versus* H^{-1} *gives values for* $M_{SAT}(T)$. *Data for 14, 42, 80 and 160 K are shown.*

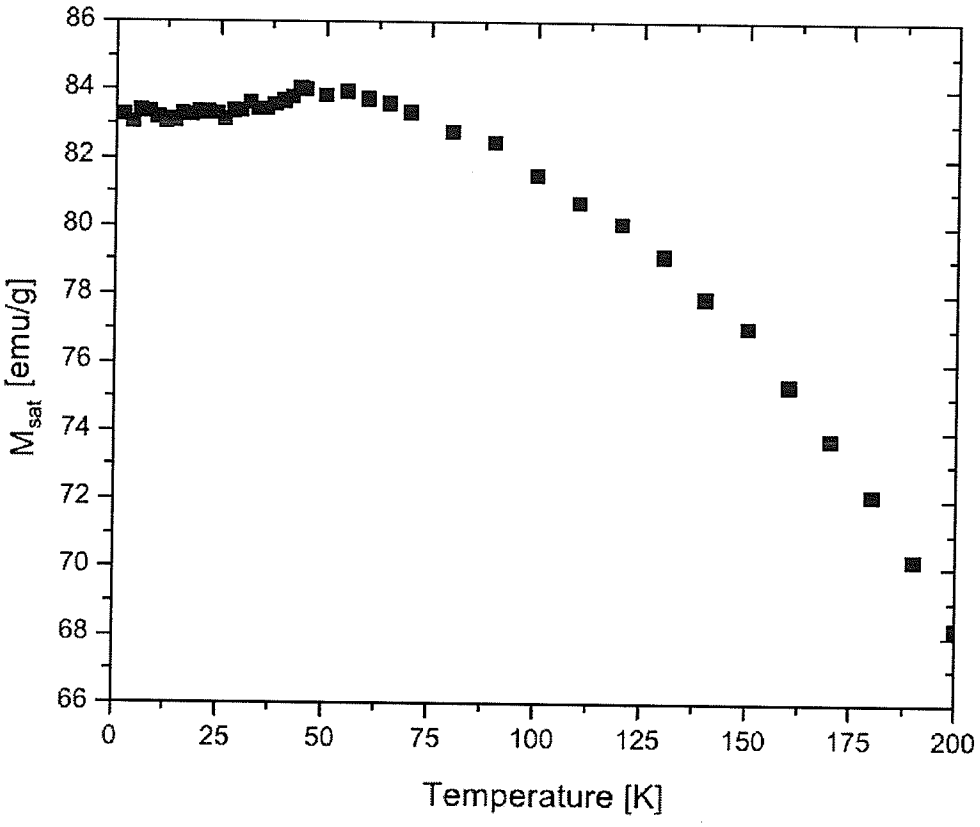

Figure 5.14: *Summary of* $M_{SAT}(T)$ *values.*

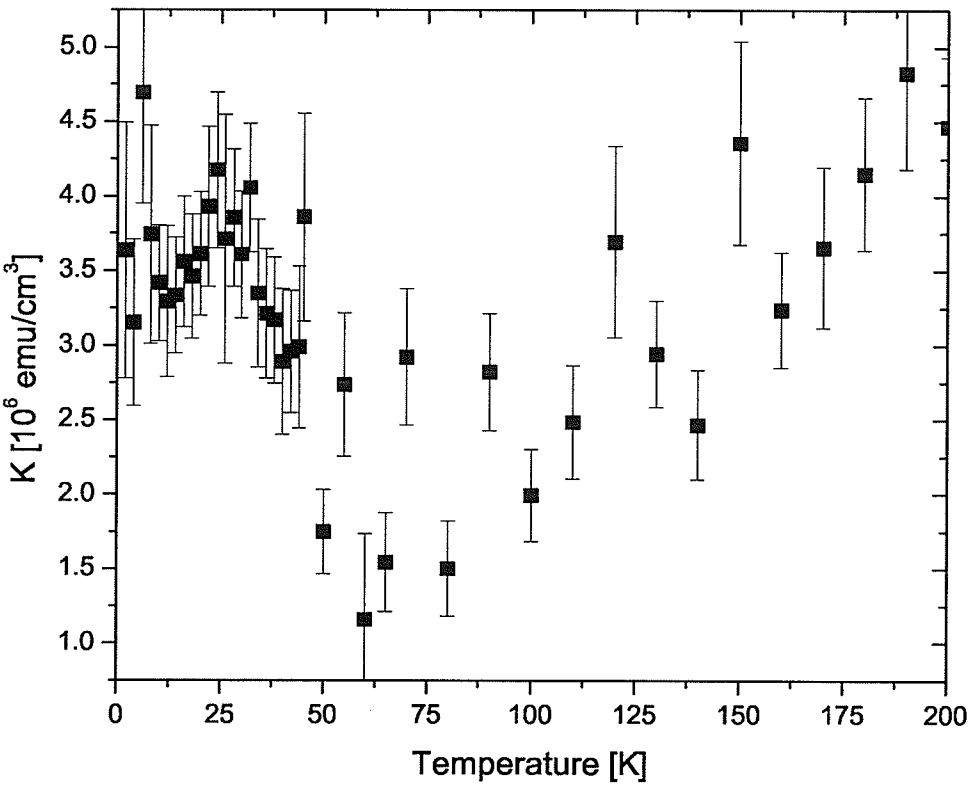

Figure 5.15: *Magnetic anisotropy obtained from approach to saturation using Eq.* (9).

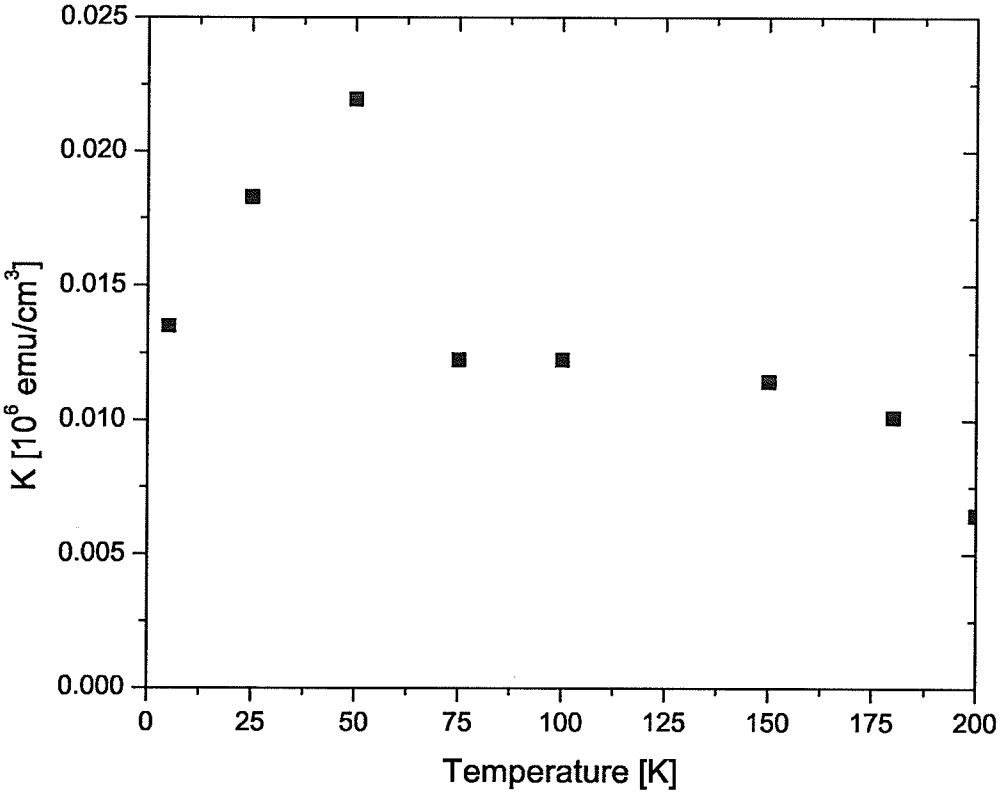

Figure 5.16: *Magnetic anisotropy obtained from coercive field data using Eq.* (10). *Error bars are estimated to be the same size as the data points.*

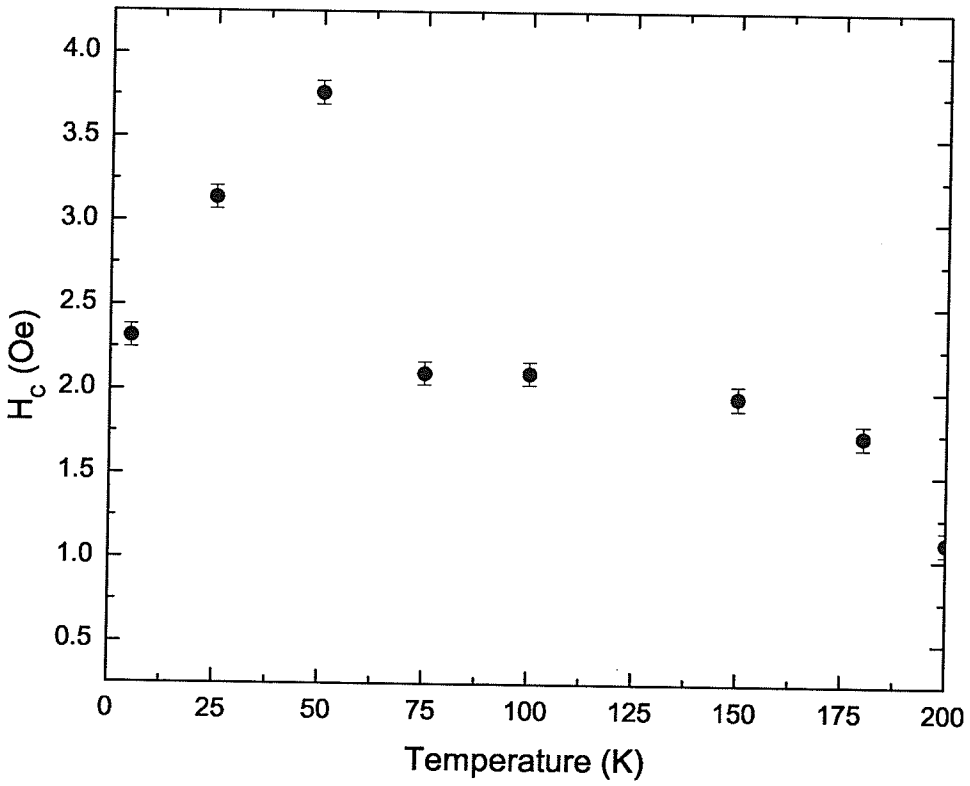

Figure 5.17: *Coercive field data from Senchuk et al. [31].*

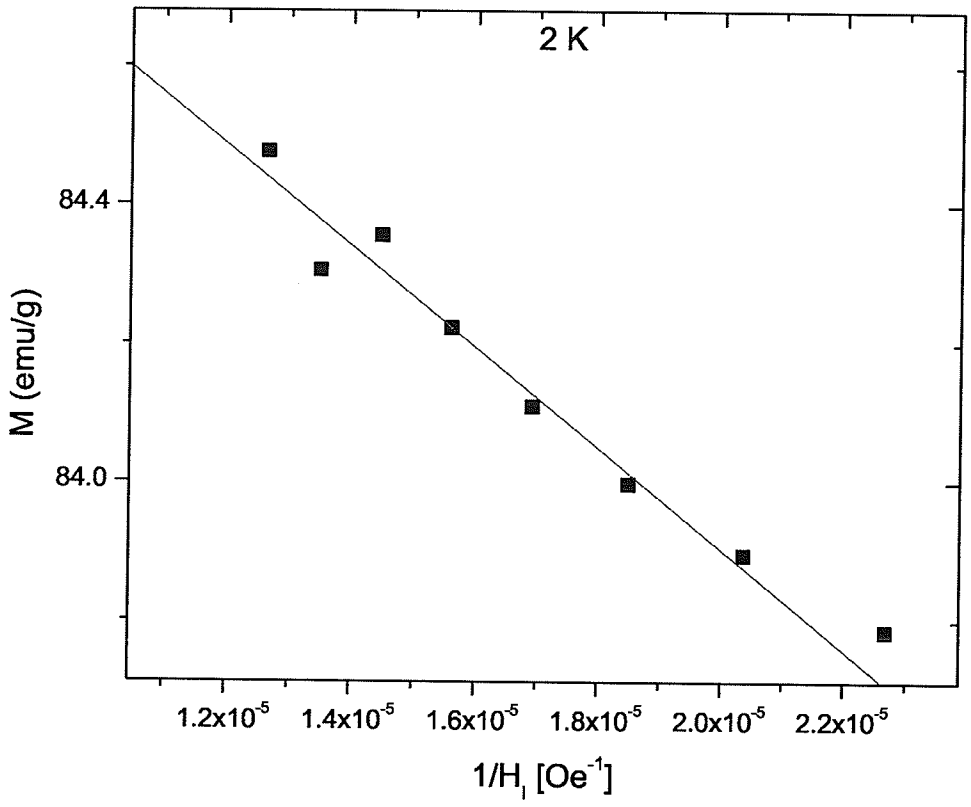

Figure 5.18: *$M_{SAT}(0)$ obtained by extrapolating magnetization versus H^{-1} at 2 K to $H^{-1} = 0$.*

5.2 Data for $La_{0.5}Sr_{0.5}CoO_3$

5.2.1 Data Acquisition

The data describing the approach to magnetic saturation for the $La_{0.5}Sr_{0.5}CoO_3$ sample were obtained using a similar method to that used for the $La_{0.73}Ba_{0.27}MnO_3$ sample. The data, shown in Figure 5.19, were taken over a temperature range from 5-260 K with the magnetic field varying from 20-80 kOe.

5.2.2 Fitting the Data

The data were fitted using the protocol developed for the $La_{0.73}Ba_{0.27}MnO_3$ sample. Sample data and summaries for b(T), $\chi(T)$, and $M_{SAT}(T)$ are shown in Figures 20-26.

One may argue that the fitting procedure described above is incorrect for the polycrystalline $La_{0.5}Sr_{0.5}CoO_3$, as a(T) was set to zero based on the fact that the previous sample was single crystal with few inhomogeneities, which is not true for the polycrystalline sample. It turns out that the $\frac{1}{H^2}$ term dominates for fields $H \gg 4\pi M_{SAT} \approx 0.3 - 0.6\ T$ [18]. The fitting regime used in this study covers much higher field strengths, thus making the exclusion of a(T) acceptable. Also, it is not possible for the H^{-1} term to remain valid at arbitrarily high fields [20].

The fitting employed by Mira et al [33] was also considered, where the derivative of Eq. (7) is taken such that

$$\left(\frac{dM_H}{dH} - \chi\right) \cdot H^3 = aH + 2b.$$

This method was not used, as a lot of noise was present in the data while the fits from the previous method are relatively smooth.

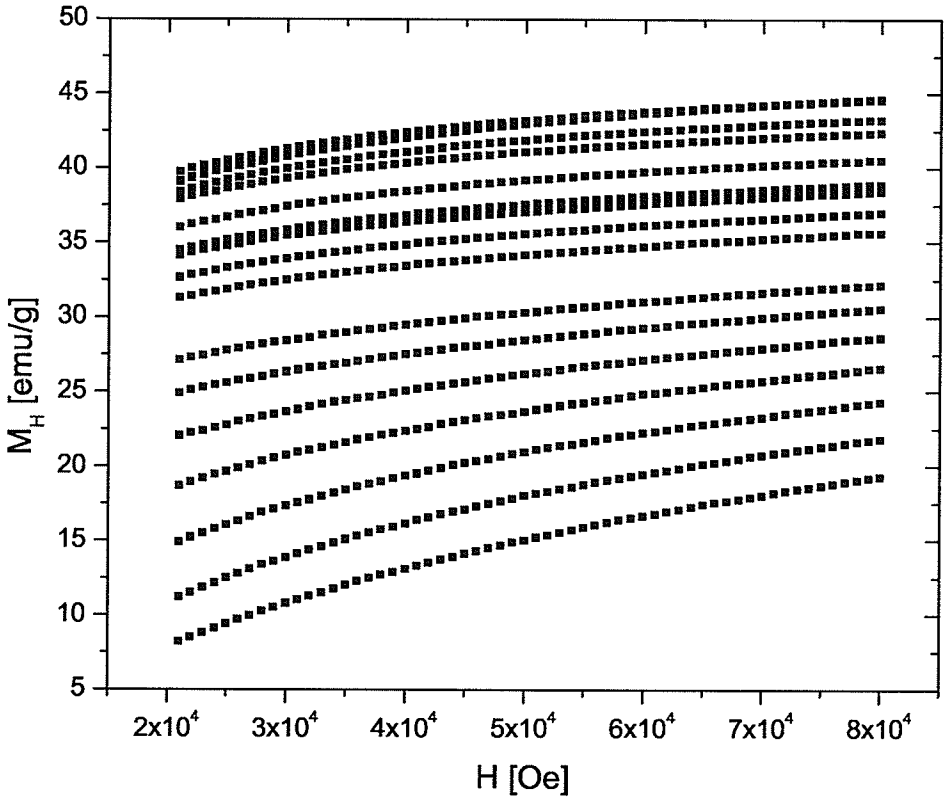

Figure 5.19: *Data for $La_{0.5}Sr_{0.5}CoO_3$. Data were measured for temperatures of 5, 25, 50, 75, 100, 120, 140, 150, 160 and 175 K. Data were also taken in 10 K steps from 200-270 K. Lower temperature data are at the top of the graph.*

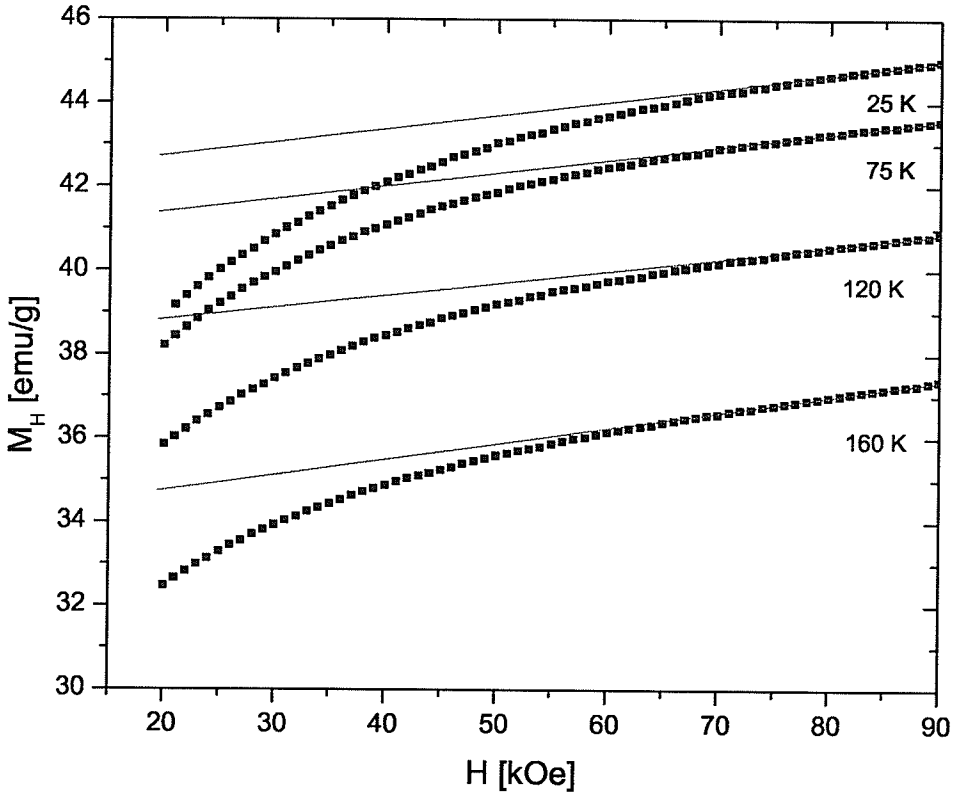

Figure 5.20: $\chi(T)$ *found from high field slopes. Data are shown for 25, 75, 120 and 160 K.*

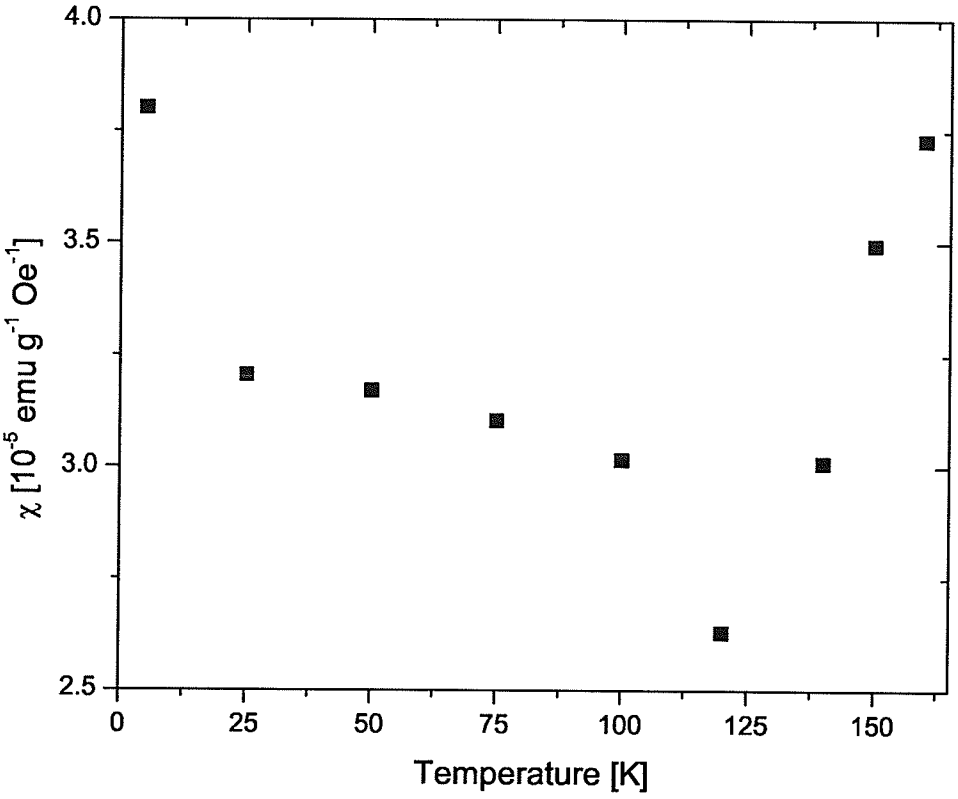

Figure 5.21: *Summary of $\chi(T)$ values.*

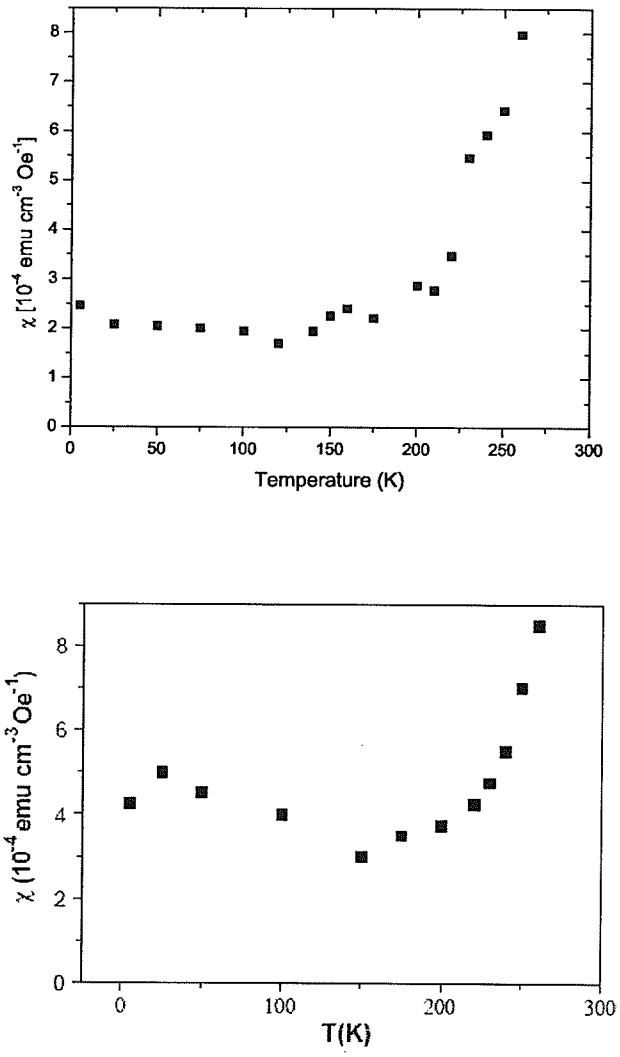

Figure 5.22: *Experimental $\chi(T)$ values (above) shown with data from Mira et al [33] (below) for comparison.*

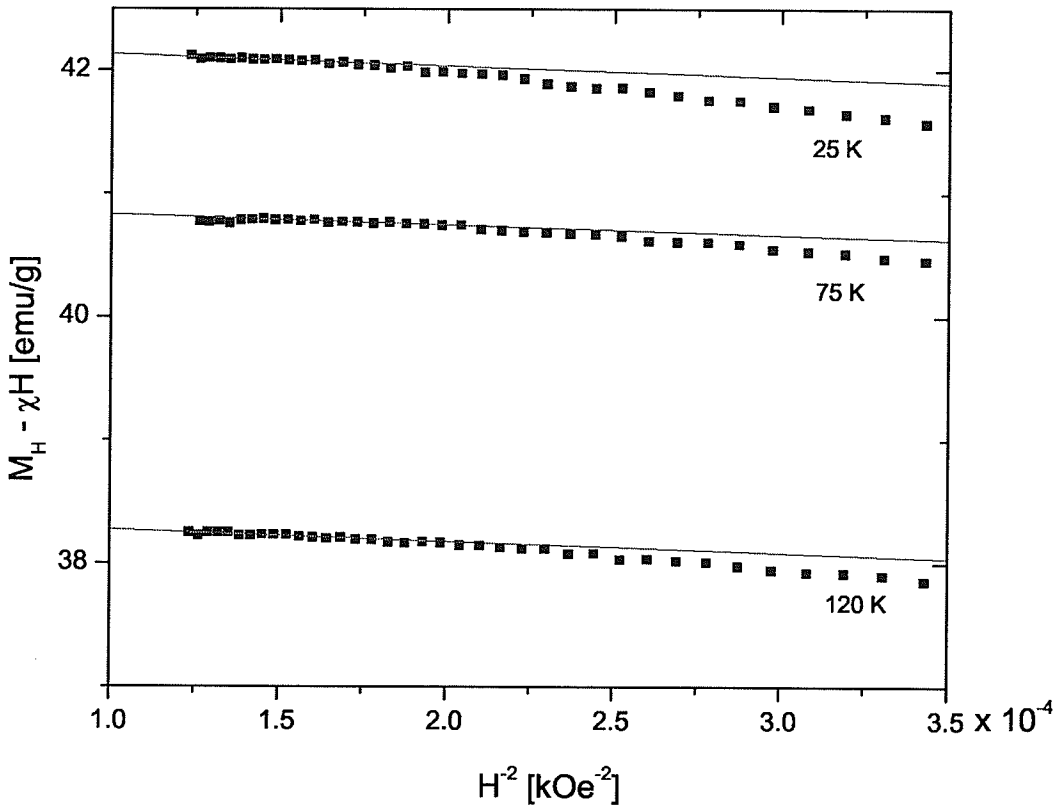

Figure 5.23: *b(T) found from* $M - \chi(T) \cdot H$ *versus* H^{-2}*. Data are shown for 25, 75 and 120 K.*

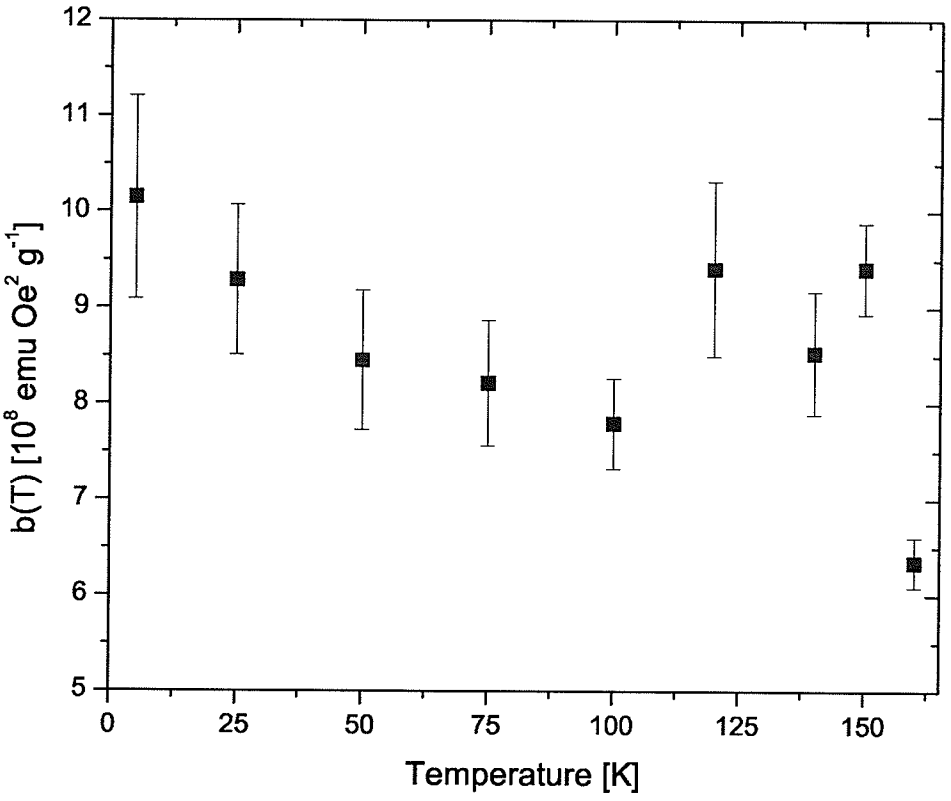

Figure 5.24: *Summary of b(T) values.*

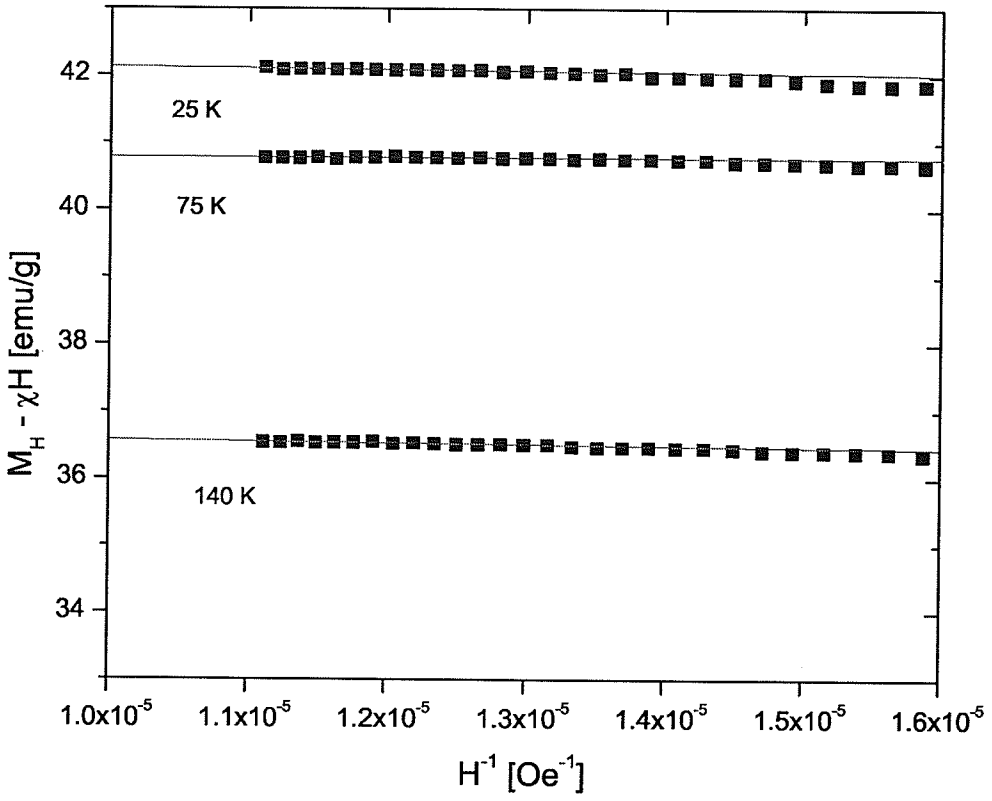

Figure 5.25: *$M_{SAT}(T)$ obtained from the y-intercept of $M - \chi(T) \cdot H$ versus H^{-1}. Data are shown for 25, 75 and 140 K.*

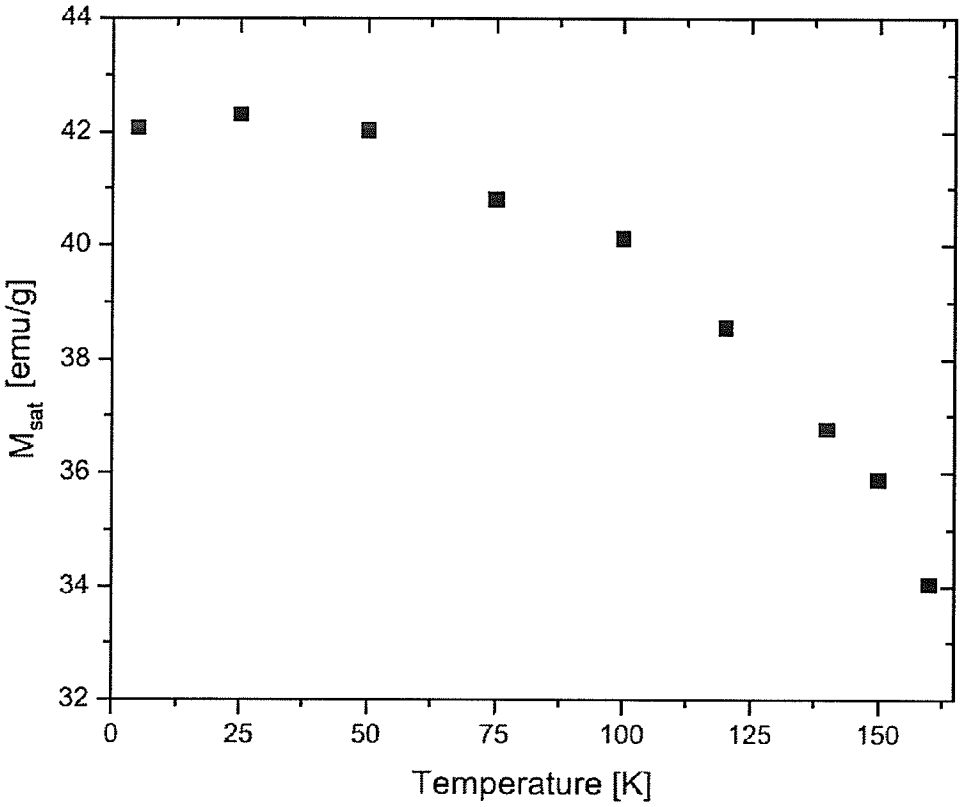

Figure 5.26: *Summary of* $M_{SAT}(T)$ *values.*

5.2.3 Magnetic Anisotropy

Magnetic anisotropy was plotted for the $La_{0.5}Sr_{0.5}CoO_3$ sample using Eq. (9) and Eq. (10) shown in Figures 5.27 and 5.28 respectively. The coercive field data shown in Figure 29 was again obtained from Senchuk et al. [31]. The value $\alpha = \frac{8}{105}$ was used again and is an acceptable value for polycrystalline samples with cubic symmetry as deduced in Appendix A. As in Eq. (10) was again set to 0.1 to obtain a maximum value for K(T). Data from Mira et al are shown in Figure 5.30 for comparison.

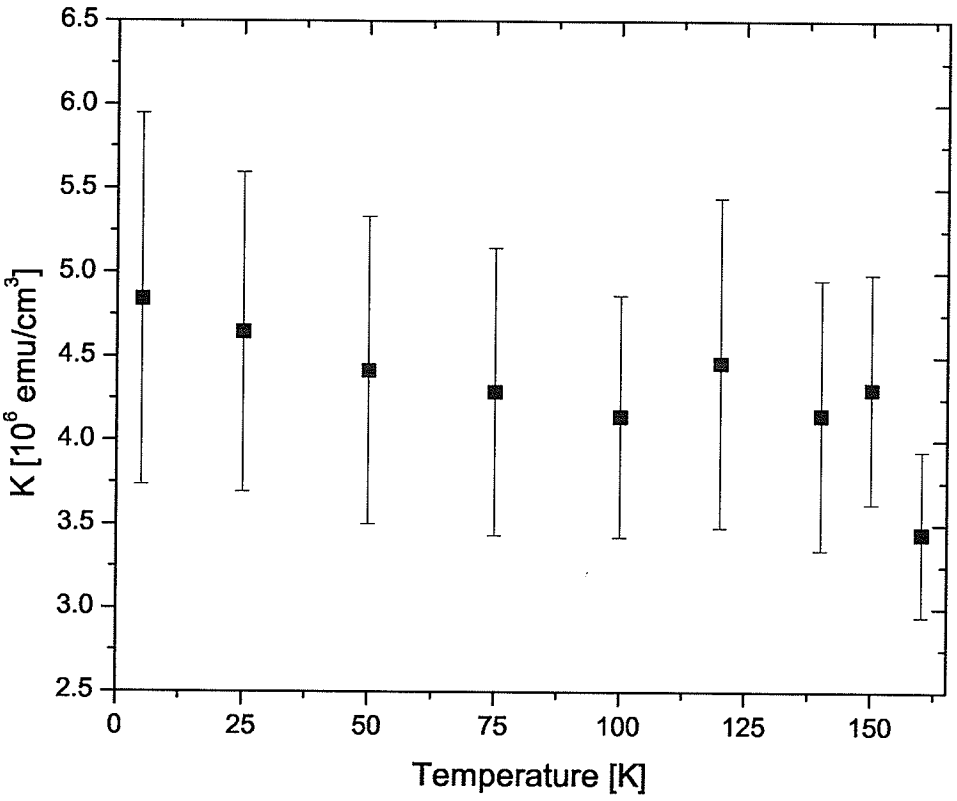

Figure 5.27: *Magnetic anisotropy from approach to saturation using Eq.* (9).

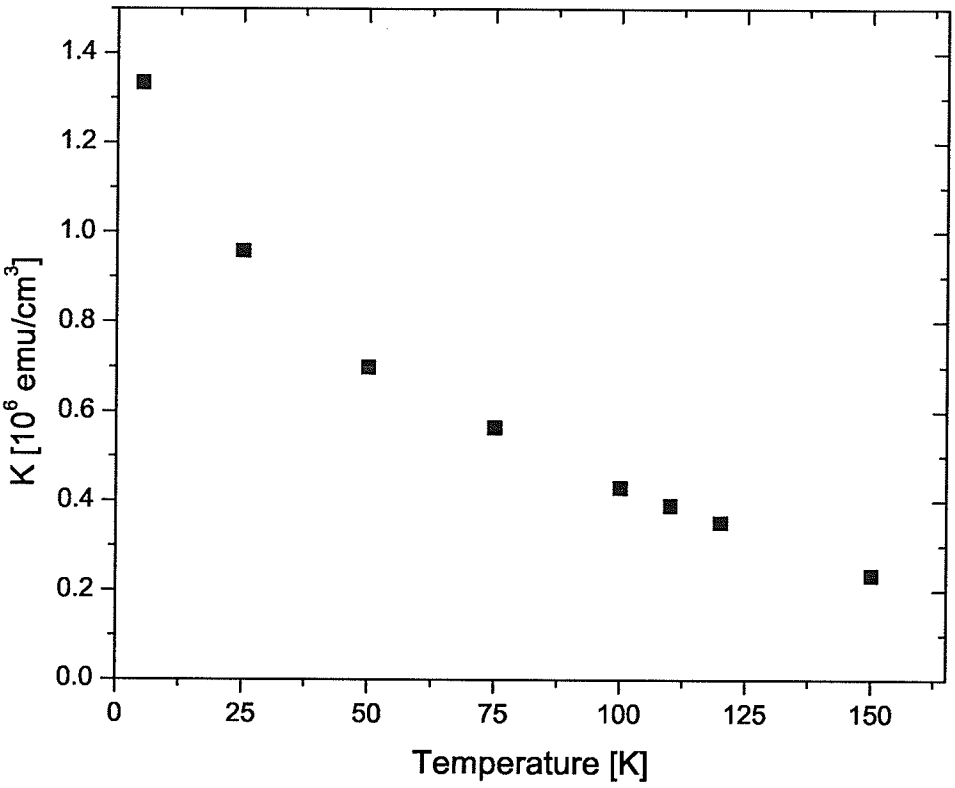

Figure 5.28: *Magnetic anisotropy from coercive field data using Eq.* (10), *with* $A = 0.1$.

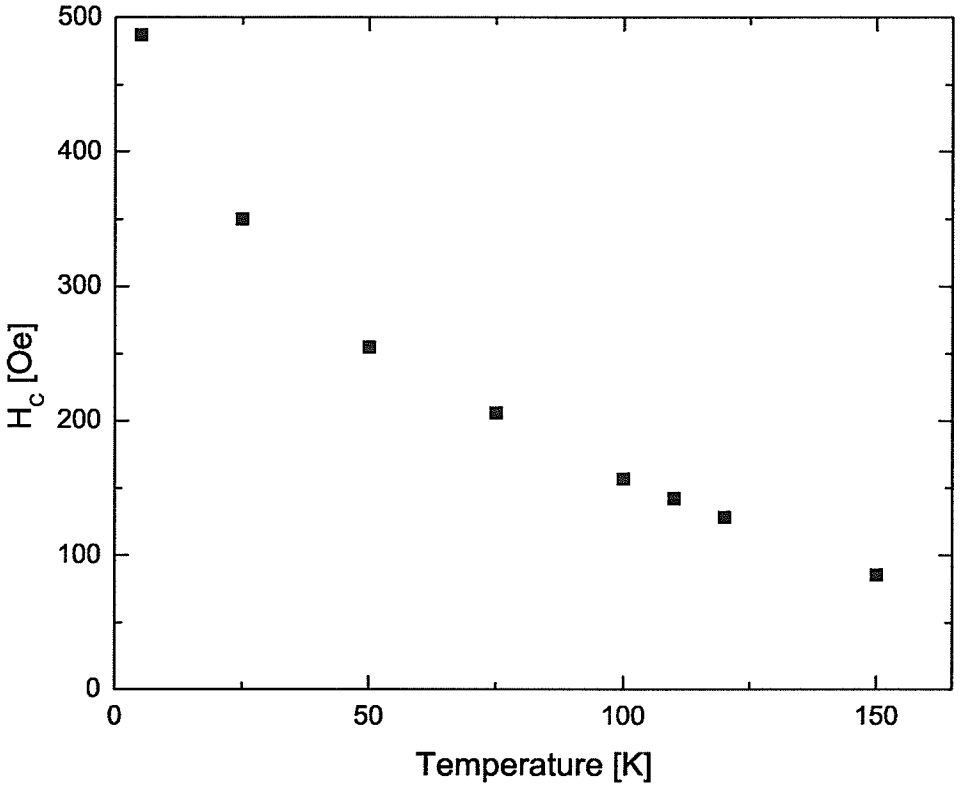

Figure 5.29: *Coercive field data.*

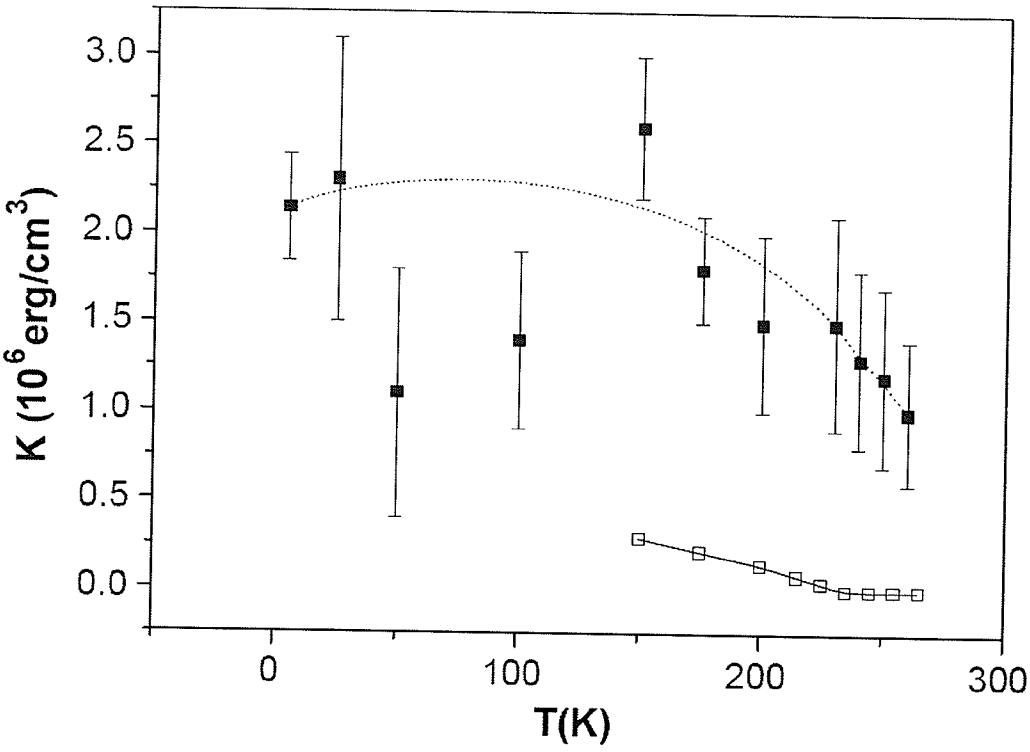

Figure 5.30: *Mira et al [33] data for K(T) found from b(T) (closed symbols) and coercive field (open symbols)*

Chapter Six

6 Analysis and Conclusion

6.1 Reduction of Spontaneous Magnetization in $La_{0.73}Ba_{0.27}MnO_3$

Analysis

The data in Figure 5.14 show a marked reduction in the spontaneous magnetization at temperatures below 60 K. The data were fit using the spontaneous magnetization formula derived from spin-wave theory Eq. (4)

$$\frac{M_S(T)}{M_S(0)} = 1 - \left(\frac{T}{4T_C}\right)^{3/2} \cdot \zeta\left(\frac{3}{2}, \frac{\Delta}{k_B T}\right).$$

while D can be found from

$$D = \frac{k_B T_C}{\pi}\left(\frac{1}{NS}\right)^{2/3}$$

Using these equations, the data between 60 K and 140 K were fit with a least squares algorithm. The best fit shown in Figure 6.1 resulted in the gap parameter, $\Delta = 0.45 \pm 0.02\ meV$ $(5.2 \pm 0.2$ K) and $D = 65.7 \pm 2.5\ meV$ Å^2. The size of the gap parameter is consistent with analysis of heat capacity data [34] but is approximately twice the value found from neutron scattering data from $La_{0.7}Ba_{0.3}MnO_3$ [24]. While the value of D is smaller than that reported such variations have been reported in samples of $La_{1-x}Ca_xMnO_3$, with $D \approx 46\ meV$ Å^2 at $x = 0.2$ [35], which then rose to $D \approx 170\ meV$ Å^2 at $x = 0.33$ [36].

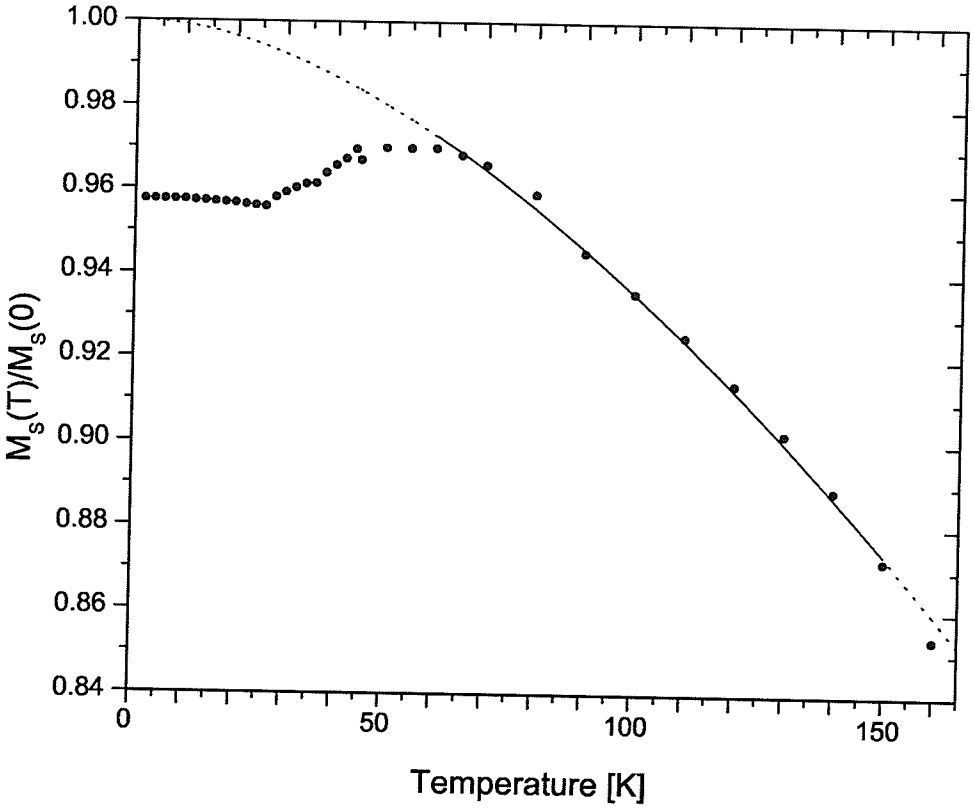

Figure 6.1: *Spontaneous magnetization fit with Eq.* (4). *The best fit is found using the parameters:* $\Delta = 0.45 \pm 0.02\, meV$ *and* $D = 65.7 \pm 2.5\, meV$ Å^2.

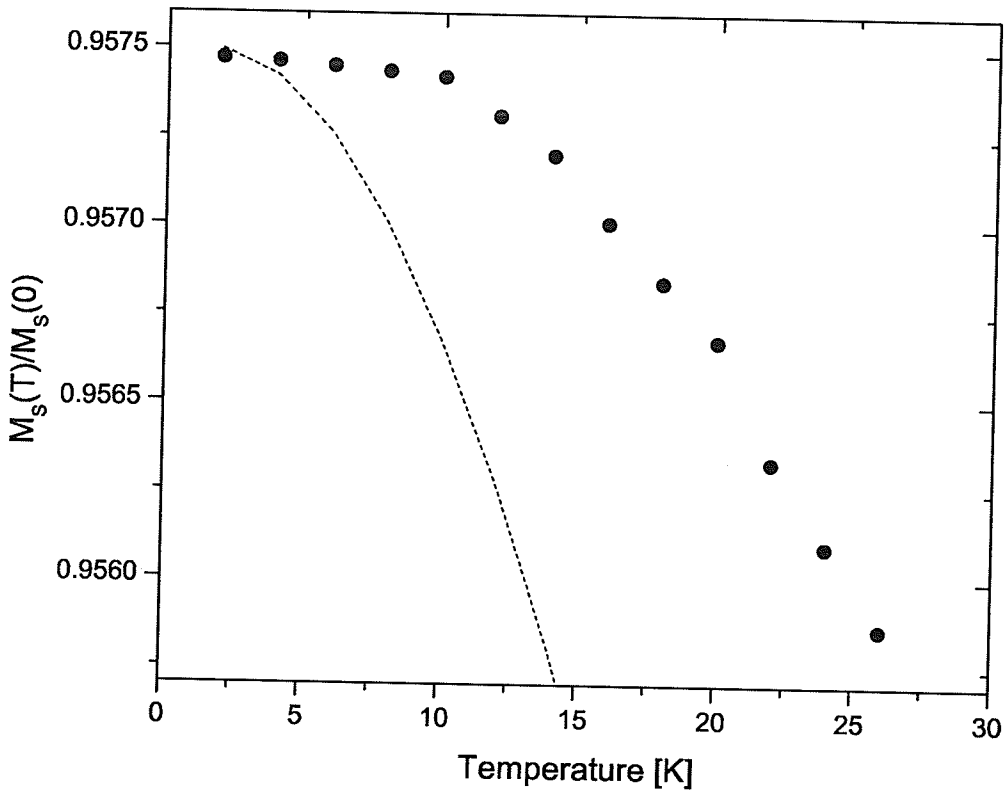

Figure 6.2: *Low temperature spontaneous magnetization data fitted using high temperature parameters found in Figure 6.1.*

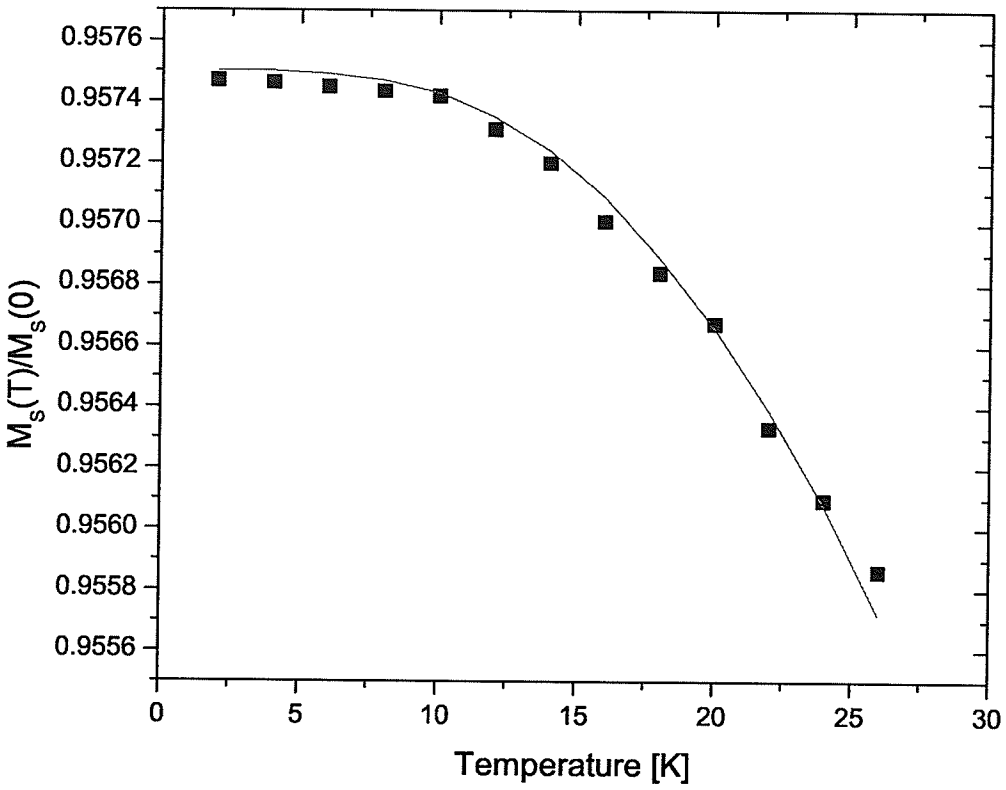

Figure 6.3: *Low temperature spontaneous magnetization data fit with* $\Delta = 2.35\ meV$ *and* D *maintained at its high temperature value.*

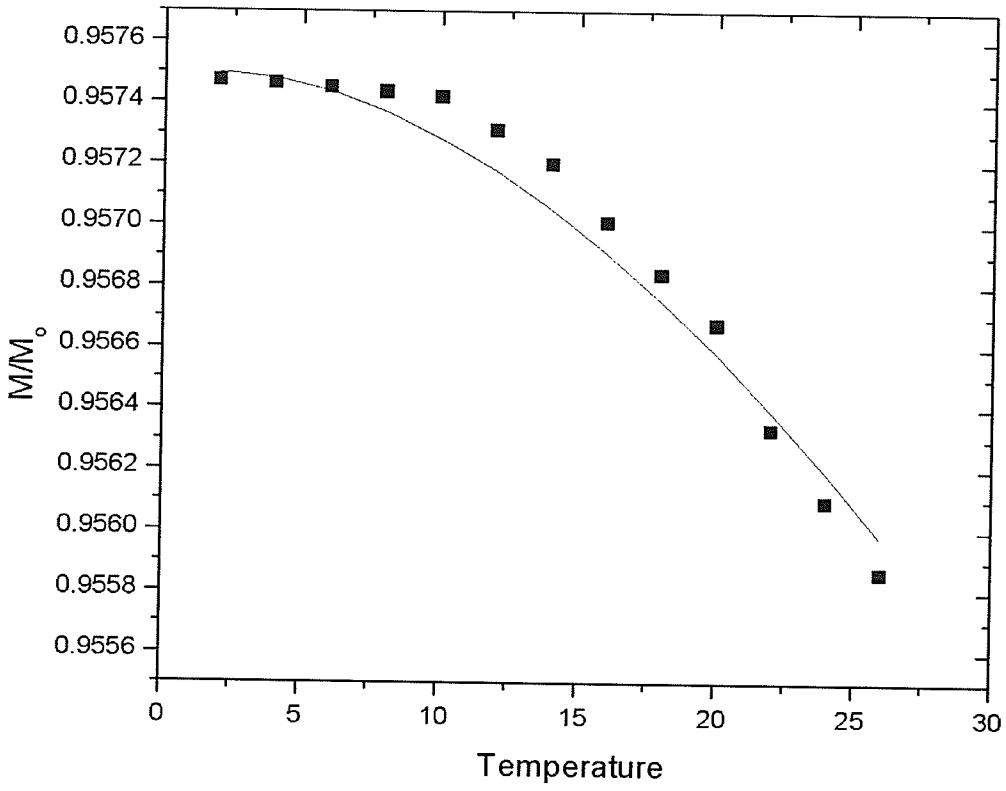

Figure 6.4: *Low temperature spontaneous magnetization data fit with* $D = 159\ meV\ \text{Å}^2$ *and* Δ *maintained at its high temperature value.*

Below 30 K, the spontaneous magnetization clearly drops from the expected value to $M_S = 0.9575(Ng\mu_B S) = 81.7(3)\ emu/g$. Figure 6.2 shows these low temperature data fit with the Δ and D values obtained from the above 60 K fits. The fit is obviously more temperature dependent than the data. Figure 6.3 shows the data fit with D maintained at it's previous value, while Δ has been varied. A value of $\Delta = 2.35\ meV$ (27.2 K) is obtained.

Figure 6.4 show the same data fit, this time maintaining Δ at it's original value and allowing D to vary. A value of $D = 159\ meV\ \text{Å}^2$ is obtained.

Due to the limited low temperature data available, as well as the relative flatness of the data, it was not possible to fit for both Δ and D independently.

Conclusion

Although it provides the better fit, present work shows that gap parameters on the order of 5 K are higher than consensus values, let alone the 25 K found above. Though this new fit may not be acceptable physically, one cannot argue against the reduction in moment. This reduction is consistent with spin canting, resulting in a canting angle of 17° ($\theta = \cos^{-1}[0.958]$). The reduction may also be caused by the formation of a spiral magnetic structure along an axis parallel with the external field, with a similar angle. The measurements made in this experiment being macroscopic, cannot differentiate between these various microscopic mechanisms.

Structural changes discussed in Chapter 3 have been shown to cause a moment reduction in $La_{1-x}Ba_xMnO_3$ with compositions of $x = 0.2$ [25, 26] and $x = 0.33$ [27] a range which includes the studied composition. This reduction occurs between the higher temperature/higher moment R3c phase and the lower temperature Pbnm/Imma phase. This structural change has been shown quite clearly in neutron scattering data and occurs around 200 K. It is linked to a decline in the ac

susceptibility, $\chi_{ac}(0,T)$ which can be seen in Figure 6.6.

An additional feature in the $\chi_{ac}(0,T)$ plots (Figure 6.6) that needs to be identified is the second decrease that occurs around 100 K and ends at 50 K. This decline contrasts with those reported in other ferromagnets where the Hopkinson maximum (a peak in χ_{ac} just below T_C followed by a rapid decline in this property with decreasing temperature, similar to that seen in near 240 K in Figure 6.5), arises from technical magnetic sources such as domain wall motion. The Hopkinson maximum occurs when the coercive field, $H_C(T)$, is greater than the ac driving field as $H_C(T)$ increases in temperatures below T_C. $H_C(T)$ is considered to be a direct reflection of the technical magnetic behaviour.

If $\chi_{ac}(0,T)$ were to be controlled by technical processes, it would correlate approximately with the inverse of $H_C(T)$, as illustrated schematically below.

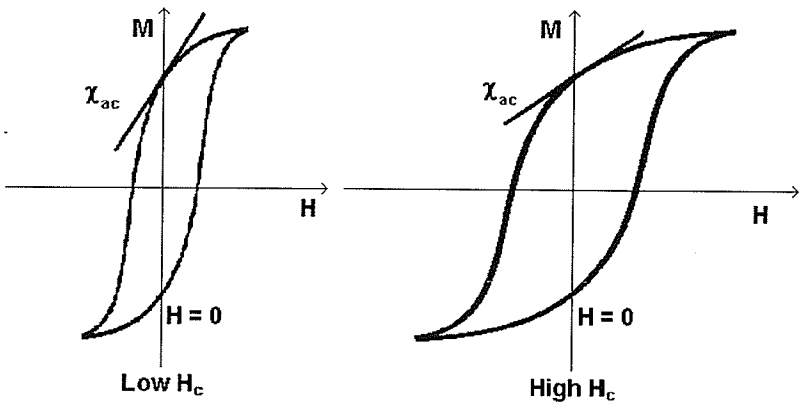

Figure 6.5: *A schematic representation of how χ_{ac} would correlate with the inverse of $H_C(T)$.*

Figures 6.7 and 6.8 display χ_{ac} and $H_C(T)$, it is quite evident that this correlation does not exist. $H_C(T)$ exceeds the ac driving field of 0.1 Oe by essentially an order of magnitude everywhere below T_C and also, the value of χ_{ac} in the liquid helium

temperature range would have to be around the value it obtains at 150 K, which it obviously does not.

The zero-field cooled (ZFC) data shown in Figure 6.9 also demonstrate the same two step decrease shown in $\chi_{ac}(0,T)$, but was acquired at field ranges much greater than those of $H_C(T)$ (30-100 Oe). ZFC data is obtained when the sample temperature is lowered to the measured value in zero magnetic field, and once that temperature has been reached the field is turned on.

The two step decrease is also present in $\chi_{ac}(H,T)$ shown in Figure 6.7. It is tempting to attribute the field induced suppression that occurs below 60 K to domain wall pinning, as done in a variety of other systems; However studies on the $La_{0.8}Ba_{0.2}MnO_3$ [25] discussed in Chapter 3 also displayed the two step decrease but showed no frequency dependence in the response at temperatures below 50 K, which would occur if pinning were present.

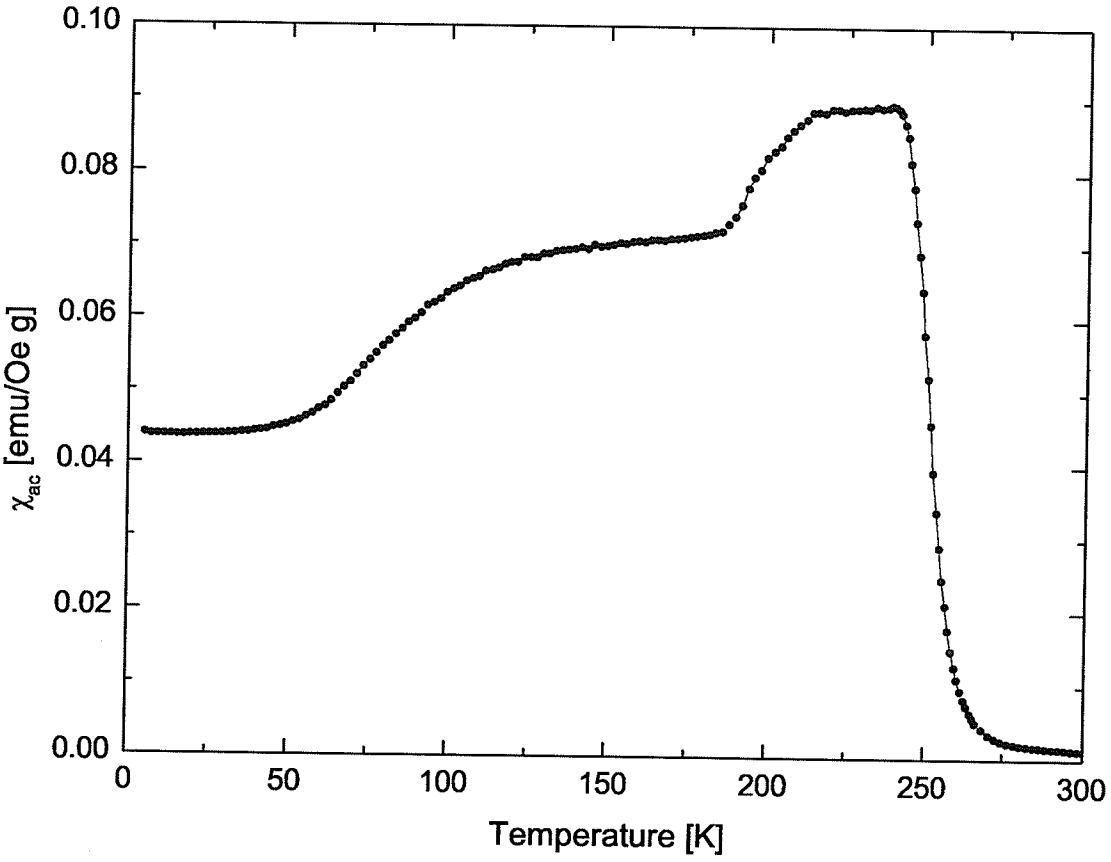

Figure 6.6: $\chi_{ac}(0,T)$ *for single crystal* $LaBaMnO_3$.

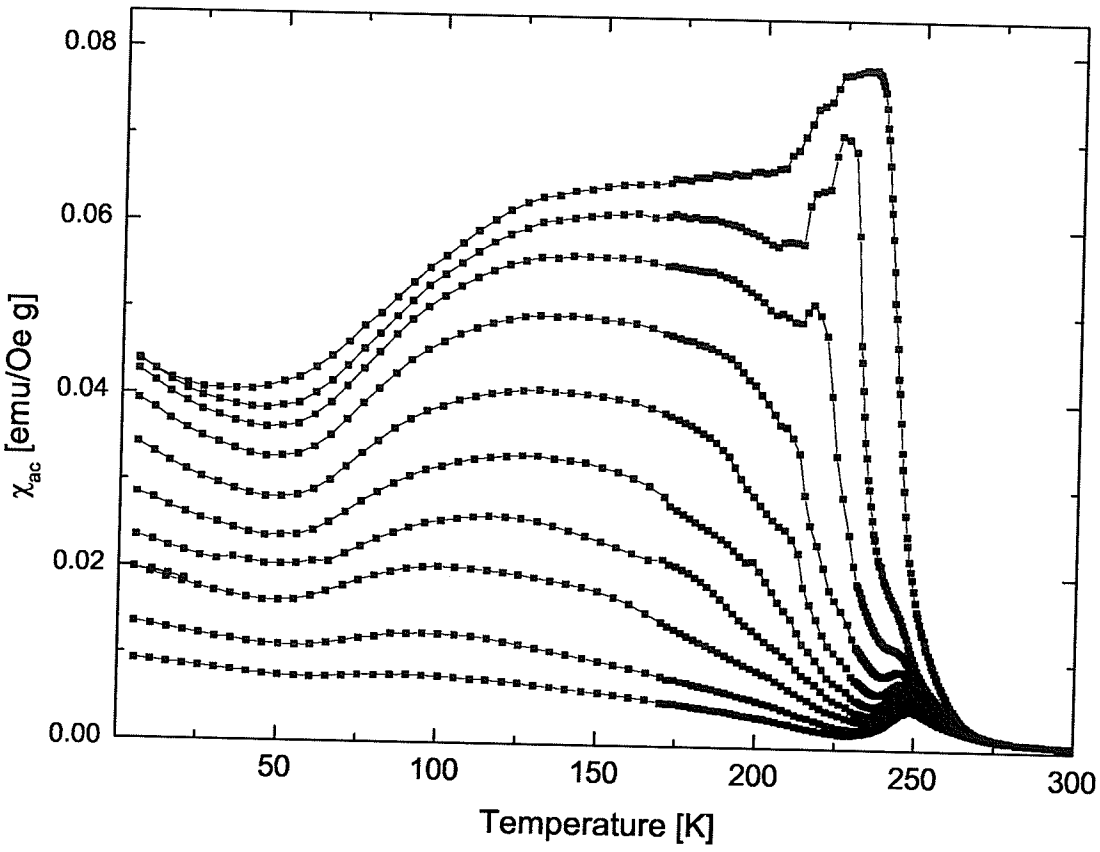

Figure 6.7: $\chi_{ac}(H,T)$ *for* $LaBaMnO_3$. *Data are shown for applied fields of 200 (top), 400 - 1000 in 100 Oe steps, 1200 and 1400 Oe (bottom).*

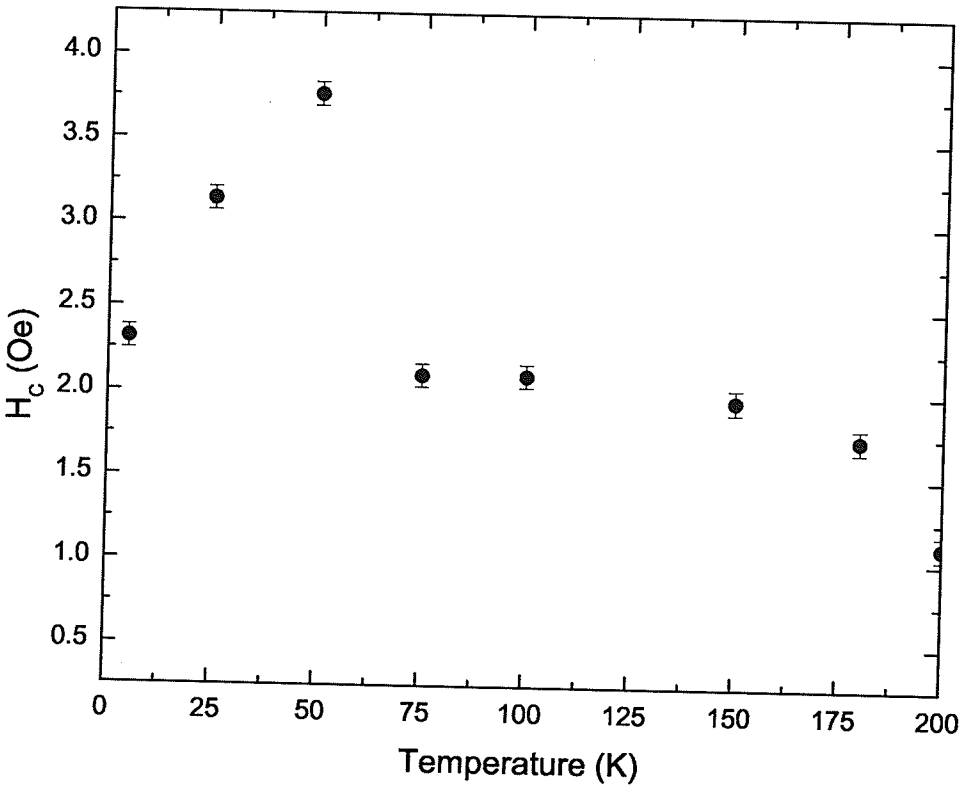

Figure 6.8: *Coercive field data for* $LaBaMnO_3$.

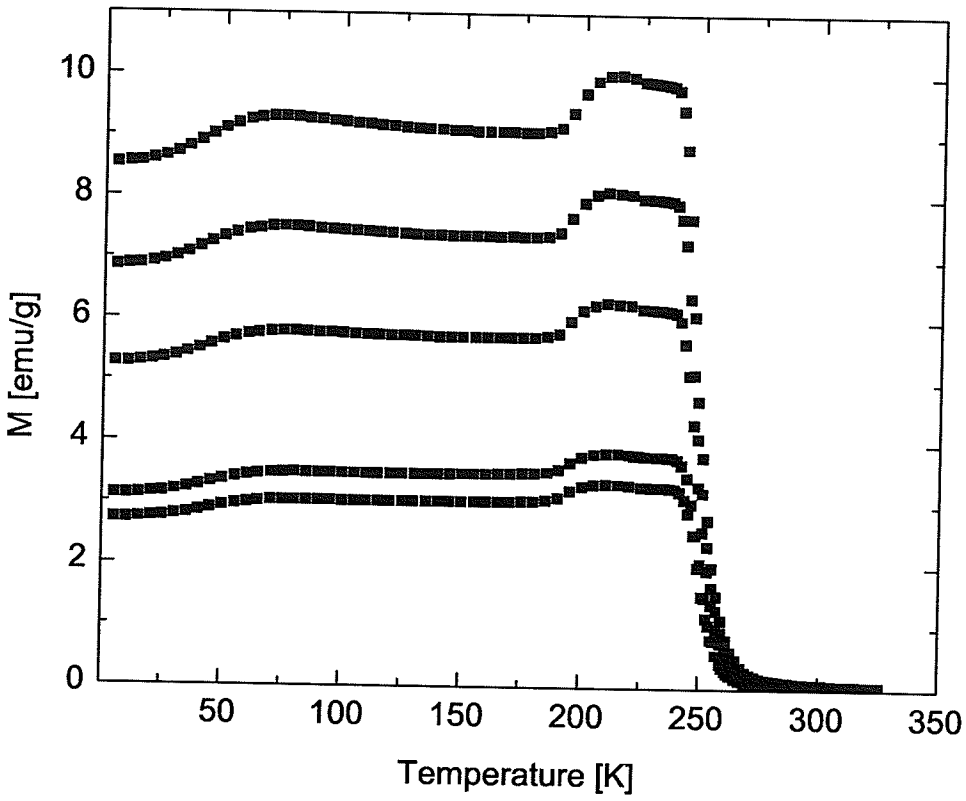

Figure 6.9: *Zero-field cooled data for $LaBaMnO_3$. Data are shown for 100 (top) - 40 Oe in 20 Oe steps and 30 Oe (bottom).*

The three arguments presented above support the suggestion that the decrease in χ_{ac} around 100 K ending in a plateau near 50 K in $\chi_{ac}(0,T)$, which correlates with reduction in moment, is not technical in nature.

A second structural phase change below 100 K could possibly be responsible for the reduction in moment, but recent measurements on thermal expansion in single crystals of $x = 0.2$ and $x = 0.3$ show that while there is an anomaly near 175 K in the lower composition linked to the R3c to Pbnm/Imma phase change, this phase change is barely visible in the higher composition, which is closer to that studied here. Also, neutron data, which would show the phase change more clearly yield no indication of a second structure change down to 5 K and thus provide good evidence that the Pbnm/Imma phase is stable throughout the region of interest. Temperature dependent X-ray data would be useful to confirm this, but the equipment is not presently available for such a study.

In summary, it has been shown that a reduction in the spontaneous magnetization takes place around 50 K. Arguments show that the reduction is probably not associated with structural phase change or technical magnetic processes. Further investigations into the microscopic and atomic spin arrangement of the $La_{1-x}Ba_xMnO_3$ $(0.2 \leq x \leq 0.3)$ at low temperatures would therefore be desirable.

6.2 Magnetic Anisotropy in $La_{0.73}Ba_{0.27}MnO_3$ and $La_{0.5}Sr_{0.5}CoO_3$

Background

In a recent paper, Mira et al. [33] measured the magnetic anisotropy of $La_{0.7}Sr_{0.3}CoO_3$. They found the magnetic anisotropies calculated from the high field slope of the magnetization curve to be an order of magnitude higher than those calculated from the coercive field data when the values should be of a similar magnitude. In order to explain this effect, they looked to the work of Ibarra et al. [37] who measured a huge magnetorestriction in $La_{1-x}Sr_xCoO_3$ with $x = 0.3$ and $x = 0.5$. In order to explain this large discrepancy Mira et al. proposed that the application of an external field causes a "Jahn-Teller" distortion to the Co^{3+} ion, resulting in the doubly degenerate e_g state splitting into two singlets ($L = 0$) and the triple degenerate t_{2g} state splitting into a singlet ($L = 0$) and a doublet ($L = 1$). The singlet state is fully occupied and the doublet level contains three electrons. A strong intra-atomic spin-orbit coupling is created due to the degeneracy in the doublet level, leading to the increase in magnetic anisotropy in an external field.

Present Work

Figures 6.10 and 6.11 show summaries of the magnetic anisotropy calculated from the high-field magnetization and coercive field data for both $La_{0.73}Ba_{0.27}MnO_3$ and $La_{0.5}Sr_{0.5}CoO_3$. It is clear that the order of magnitude discrepancy reported in the cobaltite by Mira et al. is also present in the manganite sample. The orbital instabilities that occur in the cobaltites are unlikely to appear in the manganites, so while this does not rule out the explanation provided by Mira et al. for the cobaltite, it does seem that the discrepancies might be an intrinsic feature of transition metal oxides.

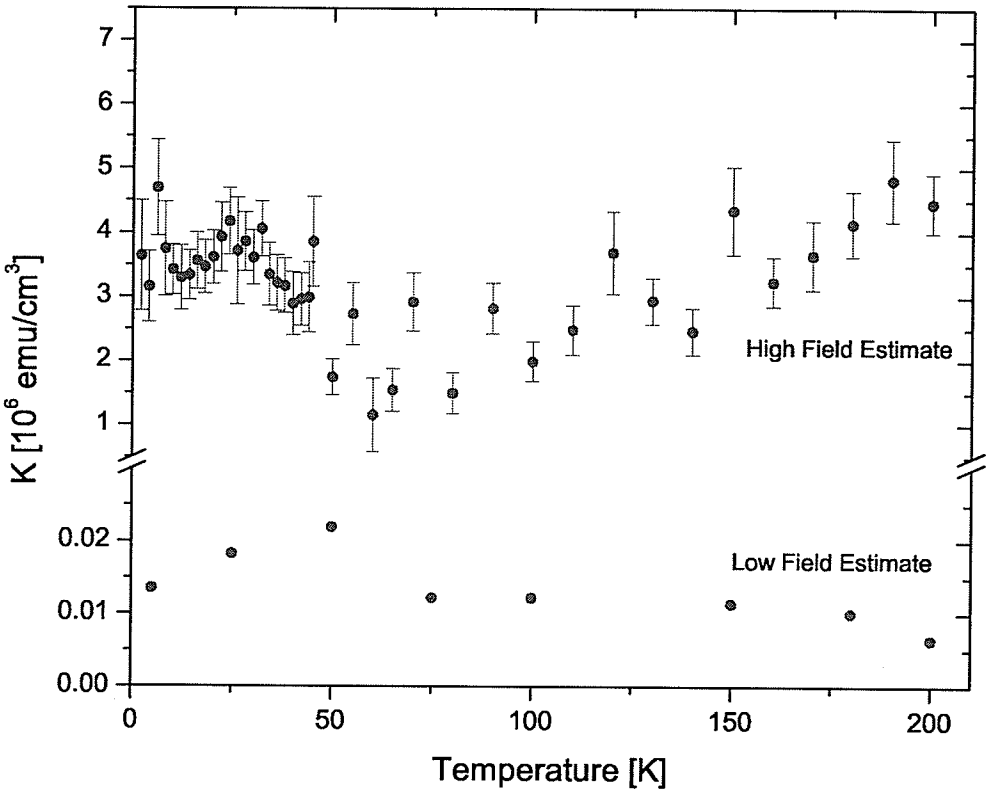

Figure 6.10: *Summary of* $K(T)$ *obtained from both Eq.* (9) *and Eq.* (10) *for* $La_{0.73}Ba_{0.27}MnO_3$.

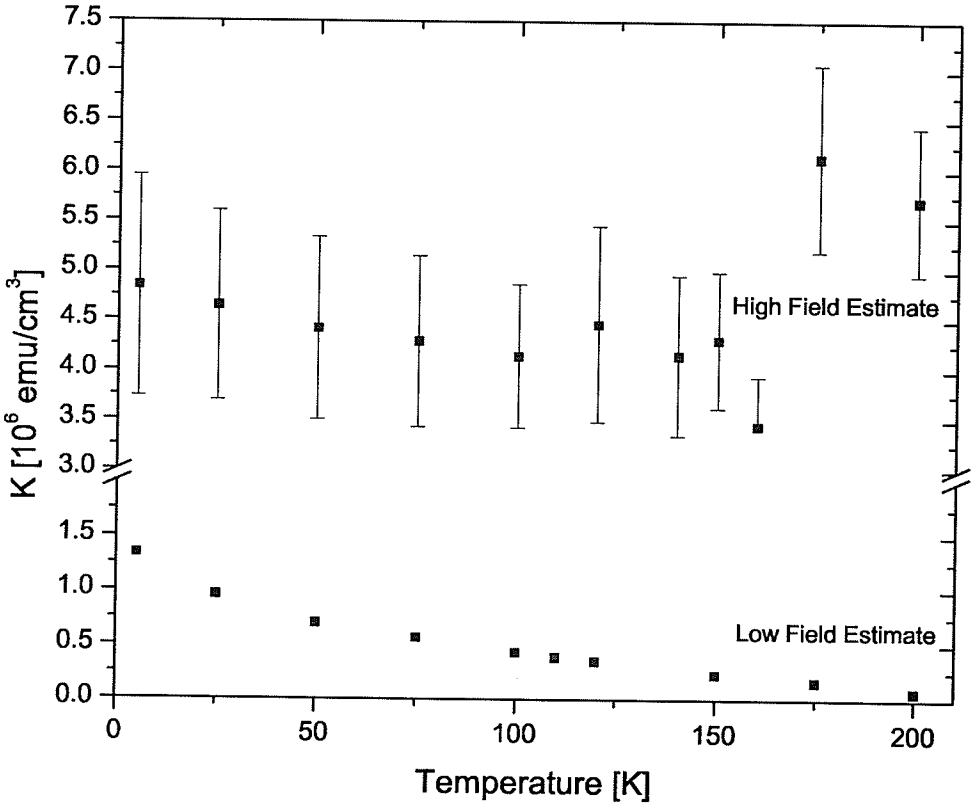

Figure 6.11: *Summary of $K(T)$ obtained from both Eq. (9) and Eq. (10) for $La_{0.5}Sr_{0.5}CoO_3$.*

6.3 Summary of Results

It was the purpose of this thesis to present the result of studies done on two samples, a manganite and a colbaltite.

Measurements of spontaneous magnetization made on the single crystal $La_{0.73}Ba_{0.27}MnO_3$ showed a marked reduction in this property below 60 K. Evidence was presented to show that this reduction was not associated with technical magnetic processes nor with a further structural phase change. Due to the macroscopic nature of the measurements made, it is not possible to determine what microscopic processes are causing this reduction.

Measurements of the approach to the saturated magnetic state were made on both the $La_{0.73}Ba_{0.27}MnO_3$ single crystal and polycrystalline $La_{0.5}Sr_{0.5}CoO_3$. From these measurements an order of magnitude difference was found between the magnetic anisotropy calculated from the high field data and that calculated from the low field coercive field data. This result agrees with a similar discrepancy found by Mira et al. [33] in the colbatite, but their explanation, based on an increase in magnetic anisotropy caused by degeneracy in the t_{2g} doublet state, does not apply to the manganites, which suggests that it may be an intrinsic feature of transition metal oxides.

A Appendix

A.1 Calculation of α

Following the approach of Chikazumi [20], the value for the geometrical constant α will be derived for cubic symmetry.

Beginning with a strong magnetic field H, a ferromagnetic material will usually become magnetized to the saturated state M_{SAT}. At this point, the magnetization M, is almost parallel to the field, differing only by a small angle θ.

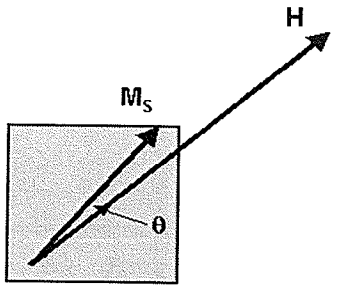

M can be can be calculated as the component of M_{SAT} in the direction of H

$$M = M_{SAT} \cdot \cos(\theta).$$

Expanding $\cos(\theta)$ leads to

$$M = M_{SAT} \cdot (1 - \frac{\theta^2}{2} + \ldots). \tag{11}$$

The torque created by H is countered by a torque from the magnetic anisotropy, given by

$$M_{SAT} \cdot H \cdot \sin(\theta) = -\frac{\partial E_a}{\partial \theta}$$

where E_a is the anisotropy energy. Assuming $\theta \ll 1$, and using the small angle

approximation, θ can now be written as

$$\theta = \left(-\frac{\partial E_a}{\partial \theta}\right)_{\theta \approx 0} \cdot \frac{1}{M_{SAT} \cdot H}$$

and Eq. (11) can be written as

$$M = M_{SAT} \cdot (1 - \frac{b}{H^2} - \ldots)$$

where

$$b = \frac{|grad\ E_a|^2}{2 \cdot M_{SAT}^2} = \frac{1}{2 \cdot M_{SAT}^2} \cdot \left[\left(\frac{\partial E_a}{\partial \theta}\right)^2 + \frac{1}{\sin^2 \theta}\left(\frac{\partial E_a}{\partial \phi}\right)^2\right] = \frac{1}{2 \cdot M_{SAT}^2} \cdot \gamma^2. \quad (12)$$

θ and ϕ are the polar coordinates of the magnetization and are related to $E_a(\beta_1, \beta_2, \beta_3)$ by the following relations:

$$E_a(\beta_1, \beta_2, \beta_3) \simeq K \cdot (\beta_1^2\beta_2^2 + \beta_1^2\beta_3^2 + \beta_2^2\beta_3^2) \quad (13)$$

$$\beta_1 = \sin\theta \cos\phi$$

$$\beta_2 = \sin\theta \sin\phi$$

$$\beta_3 = \cos\theta$$

where K is the coercive field constant. Now,

$$\frac{\partial E_a}{\partial \theta} = \frac{\partial E_a}{\partial \beta_1} \cdot \frac{\partial \beta_1}{\partial \theta} + \frac{\partial E_a}{\partial \beta_2} \cdot \frac{\partial \beta_2}{\partial \theta} + \frac{\partial E_a}{\partial \beta_3} \cdot \frac{\partial \beta_3}{\partial \theta}$$

$$= \frac{\partial E_a}{\partial \beta_1} \cdot (\cos\theta \cos\phi) + \frac{\partial E_a}{\partial \beta_2} \cdot (\cos\theta \sin\phi) - \frac{\partial E_a}{\partial \beta_3}(\sin\theta)$$

and

$$\frac{1}{\sin\theta}\frac{\partial E_a}{\partial \phi} = \frac{\partial E_a}{\partial \beta_1}\cdot\frac{\partial \beta_1}{\sin\theta\cdot\partial\phi} + \frac{\partial E_a}{\partial \beta_2}\cdot\frac{\partial \beta_2}{\sin\theta\cdot\partial\phi} + \frac{\partial E_a}{\partial \beta_3}\cdot\frac{\partial \beta_3}{\sin\theta\cdot\partial\phi}$$

$$= -\frac{\partial E_a}{\partial \beta_1}\cdot(\sin\phi) + \frac{\partial E_a}{\partial \beta_2}\cdot(\cos\phi).$$

After some algebra and simplification

$$\gamma^2 = \left(\frac{\partial E_a}{\partial \beta_1}\right)^2 + \left(\frac{\partial E_a}{\partial \beta_2}\right)^2 + \left(\frac{\partial E_a}{\partial \beta_3}\right)^2 - \left[\left(\frac{\partial E_a}{\partial \beta_1}\right)\cdot\beta_1 + \left(\frac{\partial E_a}{\partial \beta_2}\right)\cdot\beta_2 + \left(\frac{\partial E_a}{\partial \beta_3}\right)\cdot\beta_3\right].$$

Using Eq. (13) above, the derivatives are solved

$$\left(\frac{\partial E_a}{\partial \beta_i}\right) = 2\cdot K\cdot\beta_i(1-\beta_i^2)$$

and

$$\gamma^2 = 4\cdot K^2\left[(\beta_1^6+\beta_2^6+\beta_3^6) - (\beta_1^8+\beta_2^8+\beta_3^8) - 2\cdot(\beta_1^4\beta_2^4+\beta_2^4\beta_3^4+\beta_3^4\beta_1^4)\right].$$

Averaging over all possible orientations of a polycrystalline material gives

$$avg(\beta_i^6) = \frac{1}{7},\ avg(\beta_i^8) = \frac{1}{9},\ avg(\beta_i\beta_j) = \frac{1}{105}$$

which, when substituted into γ^2 and inserted into Eq. (12) gives the result

$$b = \frac{8}{105}\frac{K^2}{M_{SAT}^2},$$

which, when compared to Eq. (8) gives the value of α to be

$$\alpha = \frac{8}{105}.$$

References

[1] A.P. Ramirez, *J. Phys.: Condens. Matter* **9**, 8171 (1997)

[2] G.H. Jonker and J.H. Van Santen, *Physica* **16**, 337 (1950)

[3] J.H. Van Santen and G.H. Jonker, *Physica* **16**, 599 (1950)

[4] C. Zener, *Phys. Rev.* **82**, 403 (1951)

[5] P.G. De Gennes, *Phys. Rev.* **118**, 141 (1960)

[6] P.W. Anderson and H. Hasegawa, *Phys. Rev.* **100**, 675 (1955)

[7] J. Kanamori, *J. Appl. Phys. (Suppl.)* **31**, 145 (1961)

[8] J.B. Goodenough, *Magnetism and the Chemical Bond* (N.Y. - London, 1963)

[9] L.M. Rodriquez-Martinez and J.P. Attfield, *Phys. Rev. B* **54**, 15622 (1996)

[10] A. Moreo, M. Mayr, A. Feiguin, S. Yunoki and E. Dagotto, *Phys. Rev. Lett.* **84**, 5568 (2000)

[11] E. Dagotto, T. Hotta and A. Moreo, *Phys. Rep.* **344**, 1 (2001)

[12] M. Uehara, S. Mori, C.H. Chen and S.W. Cheong, *Nature* **399**, 560 (1999)

[13] C. Kittel, *Introduction to Solid State Physics* (John Wiley & Sons, New Jersey, 2005) Chapter 14

[14] A.S. Alexandrov and A.M. Bratkovsky, *Phys. Rev. Lett.* **82**, 141 (1999)

[15] J.H. Zhao, H.P. Kunkel, X.Z. Zhou, G. Williams and C. Xiao, *J. Phys.: Condens. Matter* **12**, L657 (2000)

[16] F. Keffer, *Spin Waves, Handbuch der Physik XVIII/2* (Springer, Berlin, 1966)

[17] L.D. Landau and E.M. Lifshits, *Electrodynamique des Milieux Continus* (Mir, Moscou, 1969)

[18] A.H. Morrish, *The Physical Principles of Magnetism* (Krieger, New York, 1980) Chapters 6 & 7

[19] R.M. Bozorth, *Ferromagnetism* (van Nostrand, New Jersey, 1959) Chapter 11

[20] S. Chikazumi and S.H. Charap, *Physics of Magnetism* (Krieger, Florida, 1978) Chapters 7 & 13

[21] W.F. Brown, *Phys. Rev.* **60**, 139 (1941)

[22] L. Neel, *Phys. Radium* **9**, 184 (1948)

[23] E. du Tremolet de Lacheisserie, D. Gignoux and M. Schlenker, *Magnetism I - Fundamentals* (Kluwer Academic Publishers, 2002) Chapter 3

[24] T. Chatterji, L.P. Regnault and W. Schmidt, *Phys. Rev. B* **66**, 214408 (2002)

[25] V. Laukhin, B. Martinez, J. Fontcuverta and Y.M. Mukovskii, *Phys. Rev. B* **63**, 214417 (2001)

[26] V.E. Arkhipov, N.G. Bebenin, V.P. Dyakina, V.S. Gaviko, A.V. Korolev, V.V. Mashkautsan, E.A. Neifeld, R.I. Zainullina, Y.M. Mukovskii and D.A. Shulyatev, *Phys. Rev. B* **61**, 11229 (2000)

[27] A.B. Beznosov, V.A. Desnenko, E.L. Fertman, C. Ritter and D.D. Khalyavin, *Phys. Rev. B* **68**, 054109 (2003)

[28] R.V. Demin, L.I. Koroleva, R.V. Privezentsev and N.A. Kozlovskaya, *Phys. Lett. A* **325**, 426 (2004)

[29] R.V. Demin, L.I. Koroleva, and Y.M. Mukovskii, *J. Phys.: Condens. Matter* **17**, 221 (2005)

[30] P.H. Keck and M.J.E. Golay, *Phys. Rev.* **89**, 1297 (1953)

[31] A. Senchuk, H.P. Kunkel, R.M. Roshko, C. Viddal, W. Li, G. Williams and X.Z. Zhou, *Euro. Phys. J. B* **37**, 285 (2004)

[32] W. Li, H.P. Kunkel, X.Z. Zhou, G. Williams, Y. Mukovskii and D. Shulyatev, *Phys. Rev. B* **70**, 214413 (2004)

[33] M. Mira, J. Rivas, M. Vasquez, M.R. Ibarra, R. Caciutto and M.A. Senaris Rodriquez, *Europhys. Letts.* **62**, 433 (2003)

[34] J.J. Hamilton, E.L. Keatley, H.L. Ju, A.K. Raychaudhuri, V.N. Smolyaninova and R.L. Greene, *Phys. Rev. B* **54**, 14926 (1996)

[35] C.P. Adams, J.W. Lynn, V.N. Smolyaniova, A. Biswas, R.L. Greene, W. Ratcliff II, S-W. Cheong, Y.M. Mukovskii and D. Shulyatev, *Phys. Rev. B* **70**, 134414 (2004)

[36] J.W. Lynn, R.W. Erwin, J.A. Borchers, Q. Huang, A. Santoro, J.L. Peng and Z.Y. Li, *Phys. Rev. Lett.* **76**, 4046 (1996)

[37] M.R. Ibarra, R. Mahendiran, C. Marquina, B. Garcia-Landa and J. Blasco, *Phys. Rev. B* **57**, R3217 (1998)